



Gradient-based hybrid topology/shape optimization of bioinspired microvascular composites

Reza Pejman^a, Sherif H. Aboubakr^b, William H. Martin^b, Urmi Devi^b, Marcus Hwai Yik Tan^c, Jason F. Patrick^{b,*}, Ahmad R. Najafi^{a,*}

^a Department of Mechanical Engineering and Mechanics, Drexel University, Philadelphia, PA 19104, USA

^b Department of Civil, Construction, and Environmental Engineering, North Carolina State University, Raleigh, NC 27695, USA

^c Department of Mechanical Science and Engineering, University of Illinois, Urbana, IL 61801, USA

ARTICLE INFO

Article history:

Received 9 April 2019

Received in revised form 26 July 2019

Accepted 19 August 2019

Keywords:

Hybrid topology/shape optimization

Interface-enriched generalized finite element method

Microvascular composites

Active-cooling

3D printing

ABSTRACT

Construction of bioinspired vasculature in synthetic materials enables multi-functional performance via mass transport through internal fluidic networks. However, exact reproduction of intricate, natural microvascular architectures is nearly impossible and thus there is a need to create practical, manufacturable designs guided by multi-physics principles. Here we present a Hybrid Topology/Shape (HyTopS) optimization scheme for microvascular materials using the Interface-enriched Generalized Finite Element Method (IGFEM). This new approach, which can simultaneously perform topological changes as well as shape optimization of microvascular materials, is demonstrated in the context of thermal regulation. In the current study, we present a new feature that enables the optimizer to augment network topology by creating/removing microchannels during the shape optimization process. This task has been accomplished by introducing a new set of design parameters, which act analogous to the penalization factor in the Solid Isotropic Material with Penalization (SIMP) method. The analytical sensitivity for the HyTopS optimization scheme has been derived and the sensitivity accuracy is verified against the finite difference method. We impose a set of geometrical constraints to account for manufacturing limitations and produce a design which is suitable for large-scale production without the need to perform post-processing on the obtained optimum. The method is validated by active-cooling experiments on vascularized carbon-fiber composites. Finally, we compare various application examples to demonstrate the advantages of the newly introduced HyTopS optimization scheme over solely shape optimization for microvascular materials.

© 2019 Elsevier Ltd. All rights reserved.

1. Introduction

Bioinspired microvascular networks have profound potential to offer a wide range of multi-functionality to host materials by enabling internal fluid/mass transport. Fiber-reinforced polymer composites exhibit superior structural performance (e.g., high specific strength/stiffness) whereby internal vasculature provides additional functionality including self-healing, thermal regulation, electromagnetic modulation, etc. [1,2]. In this study, we focus on the thermal management capability of microvascular fiber-composites which has a broad range of applications including electric vehicle battery packaging, space re-entry and hypersonic aircraft, and heat exchangers for microelectronics [3–8].

For active-cooling applications, the geometric properties and location of internal microchannels are critical factors affecting overall cooling efficiency. Several computational approaches have been used to optimize the design of such fluidic networks, including (i) constructal theory; (ii) parametric studies; (iii) evolutionary algorithms; and (iv) gradient-based methods.

The central idea behind constructal theory [9] is that for a flow system to persist in time, the fluidic architecture must evolve in such a way that maximizes access to its currents. However, this method can only be used to solve network optimization problems that do not contain a large set of design variables and often require *a priori* information about the optimal solution.

Parametric studies are another widely used approach [10–13] that examine the impact of design parameters by performing multiple simulations. For example, Soghrati et al. minimized the maximum temperature and vascular volume fraction of an actively-cooled composite by varying the amplitude and

* Corresponding authors.

E-mail addresses: arn55@drexel.edu (A.R. Najafi), jfpatrick@ncsu.edu (J.F. Patrick).

wavelength of a sinusoidal microchannel [14]. While insightful, parametric approaches are often limited to a few design parameters due to the associated computational cost.

Evolutionary algorithms are a design methodology which adopt concepts from biological evolution. Genetic algorithms (GAs) [15] are the most widely known subset of this group. GAs are population-based algorithms that enhance a set of candidate solutions by applying genetic operators: selection, mutation, and crossover. The survival of the fittest occurs through selection, preventing the worst candidates from reproducing. This approach has been widely used for the optimization of microvascular materials [16–20]. However, there are two critical drawbacks in using GA-based approaches: (i) significant computational cost associated with the optimization; and (ii) the optimal configuration is often too complicated to manufacture [17].

Lastly, gradient-based optimization methods can be classified into two main categories: shape and topology optimization. Jarrett et al. employed gradient-based shape optimization to improve the thermal and hydrodynamic performance of batteries in an electric vehicle [21]. They prescribed pressure drop, average temperature, and thermal uniformity as the objective functions with microchannel width and position as the design parameters. More recently, Tan et al. proposed a gradient-based shape optimization scheme for actively-cooled vascular composites [4] that has been used to solve multi-objective optimization problems for battery cooling applications [22], design of nano-satellite components [23], and create microvascular networks with blockage redundancy [24]. The method builds upon the Eulerian-based shape optimization scheme proposed by Najafi et al. [25,26], which incorporates the Interface-enriched Generalized Finite Element Method (IGFEM) [27] and NURBS-based Interface-enriched Generalized Finite Element Method (NIGFEM) [28]. However, in all of these shape-based approaches, the topology of the microvascular network does not change during the optimization process.

While gradient-based topology optimization allows for reconfiguration of the material domain and is well-established for structural problems, it still needs further development for the design of fluidic networks. In an early work, Borrvall et al. applied gradient-based topology optimization for Stokes flow [29] and later extended to Navier–Stokes flow [30]. Gradient-based topology optimization has also been developed for conjugate heat transfer design problems [31], however, the computational cost of this method is substantial when solving the nonlinear Navier–Stokes equations. Recently, Zhao et al. addressed this issue by incorporating the approximate, but more efficient Darcy flow model to conjugate heat transfer [32]. They have also addressed the issue of manufacturability for the microchannel network by imposing the geometric length-scale constraint proposed in [33]. However, there is a significant difference in the pressure distribution obtained from their model compared to the nonlinear Reynolds-averaged, Navier–Stokes solution. Furthermore, they have reported difficulty in producing an interconnected fluidic network when imposing a high-pressure drop constraint.

In this study, a new scheme for gradient-based Hybrid Topology/Shape (HyTopS) optimization of microvascular materials is presented. We have extended the gradient-based shape optimization scheme proposed in [4] to simultaneously change the topology of the vascular network as well as microchannel shape within each iteration during the optimization process. This has been carried out by introducing a new set of design parameters analogous to the Solid Isotropic Material with Penalization (SIMP) method [34,35] that enables the optimizer to create/remove microchannels during the optimization process while augmenting overall topology of the network.

The analytic sensitivity proposed in [26] is employed to precisely and efficiently compute the derivatives that are required in

the gradient-based shape optimization of microvascular materials. This analytical sensitivity avoids the technical difficulties encountered in finite difference or semi-analytical schemes [36,37]. In contrast to the Lagrangian FEM-based shape optimization for which the nodal velocities need to be computed for every node in the design space, in our Eulerian IGFEM-based HyTopS optimization, only the nodal velocities of the enrichment nodes along the microchannels need to be evaluated. In other words, under the proposed method, only the enriched nodes on the boundary/interface move, appear or disappear during the optimization process.

The remainder of the paper is organized as follows. In Section 2, the IGFEM method and the dimensionally reduced thermal and hydraulic models are provided. In Section 3, the gradient-based HyTopS optimization scheme for microvascular materials and full sensitivity analysis with respect to the newly introduced design parameters are presented. An optimization outcome is experimentally validated in Section 4. Finally, in Section 5, several application problems are provided to highlight unique features of the proposed scheme.

2. Interface-enriched generalized finite element method

Two recent additions to the family of Generalized/Extended Finite Element Methods (G/XFEM), the IGFEM and NIGFEM were developed by Soghrati et al. [27,38] and Safdari et al. [28,39], respectively, to capture gradient discontinuities along material interfaces using non-conforming meshes. As opposed to the conventional G/XFEM where the generalized degree of freedoms (dofs) are associated with duplicated nodes of the non-conforming elements [40,41], the enrichment functions and the corresponding generalized dofs in IGFEM/NIGFEM are introduced along the material interfaces. Such methods were previously implemented for thermal analysis of microvascular materials [14,42]. In this section, we summarize the key concepts and notations associated with dimensionally reduced thermal and hydraulic models and IGFEM.

2.1. Dimensionally reduced thermal model for microvascular materials

As schematically shown in Fig. 1, the microvascular material is represented by domain Ω embedded with microchannels Γ_f , modeled as line sources/sinks. Considering microchannels as line sources/sinks is justified by the fact that the diameters of the microchannels are typically much smaller than the distance between them and other characteristic dimensions of the problem.

The boundary of the domain Ω is divided into two complementary subsets: Γ_T and Γ_q , over which temperature T_p and heat flux q_p'' are prescribed, respectively. Let \mathcal{K} , T , f , T_{amb} , and \dot{m} denote the thermal conductivity tensor, temperature, distributed heat source, ambient temperature, and mass flow rate, respectively. The weak form of the heat equation for a network with n_{ch} number of microchannels can be given by

$$0 = - \int_{\Omega} (\nabla v \cdot \mathcal{K} \nabla T + \tilde{h} v T) d\Omega - \sum_{j=1}^{n_{ch}} \int_{\Gamma_f^{(j)}} v \dot{m}^{(j)} c_f \mathbf{t}^{(j)} \cdot \nabla T d\Gamma + \int_{\Omega} v (f + \tilde{h} T_{amb}) d\Omega + \int_{\Gamma_q} v q_p'' d\Gamma, \quad \forall v \in \mathcal{V} \quad (1)$$

where \mathcal{V} is the space of weight functions, c_f is the coolant specific heat capacity, $\mathbf{t}^{(j)}$ is the unit tangent row vector of the microchannel j in the flow direction, and \tilde{h} is the equivalent heat loss coefficient. \tilde{h} is defined as the summation of the convection (h_{conv}) and the radiation (h_{rad}) heat transfer coefficients. The radiation heat transfer coefficient is obtained by linearizing the Stefan–Boltzmann law. It is also assumed that the in-plane conductivity is isotropic $\mathcal{K} = \kappa \mathbf{I}$, where κ is the thermal conductivity. The other assumptions

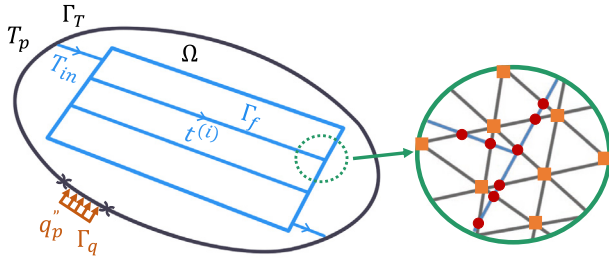


Fig. 1. Schematic of microvascular geometry and boundary conditions, with the inset showing a portion of a non-conforming mesh. Orange squares and red circles represent original and enriched nodes, respectively. (For interpretation of the references to color in this figure legend, the reader is referred to the web version of this article.)

underlying the simplified model are discussed and justified in [Appendix A](#). Due to the presence of the convective term in (1), the associated stiffness matrix is not symmetric. As explained in detail in [4], this term can lead to numerical instability at flow rates of interest in this study. This issue is mitigated by employing the Streamline Upwind Petrov–Galerkin (SUPG) stabilization method [43]. The equations associated with the SUPG method are presented in [Appendix B](#).

2.2. IGFEM formulation

As shown in [Fig. 1](#), in the IGFEM, nodes can be divided into two categories: original nodes (orange squares) and enriched nodes (red circles). Enriched nodes are defined at the intersection points between the microchannels and boundary of the elements. Using IGFEM, the temperature field in each element intersected by an interface can be approximated by

$$T^h(\mathbf{X}) = \sum_{i=1}^n N_i(\mathbf{X}) T_i + \sum_{j=1}^{n_\psi} \psi_j(\mathbf{X}) \phi_j = [\mathbf{N}(\mathbf{X}) \quad \Psi(\mathbf{X})] \begin{Bmatrix} \mathbf{T} \\ \Phi \end{Bmatrix}, \quad (2)$$

where \mathbf{X} denotes the spatial coordinates. The first term on the right-hand side of (2) represents the conventional finite element approximation by considering n standard finite element shape functions $N_i(\mathbf{X})$ and the nodal dofs T_i . The second term indicates the augmented contribution with the n_ψ enrichment functions $\psi_j(\mathbf{X})$ and their associated generalized dofs ϕ_j . In the IGFEM, generalized dofs are assigned to the enriched nodes. Details of evaluating the enrichment functions $\psi_j(\mathbf{X})$ are presented in [26].

Thermal gradients can be obtained by taking the derivative of Eq. (2) with respect to \mathbf{X} ,

$$\frac{\partial T^h(\mathbf{X})}{\partial \mathbf{X}} = \begin{bmatrix} \frac{\partial \mathbf{N}(\mathbf{X})}{\partial \mathbf{X}} & \frac{\partial \Psi(\mathbf{X})}{\partial \mathbf{X}} \end{bmatrix} \begin{Bmatrix} \mathbf{T} \\ \Phi \end{Bmatrix} = [\mathbf{B}_N(\mathbf{X}) \quad \mathbf{B}_\psi(\mathbf{X})] \begin{Bmatrix} \mathbf{T} \\ \Phi \end{Bmatrix}, \quad (3)$$

where the definition of \mathbf{B}_N and \mathbf{B}_ψ are self-evident. Implementation of the IGFEM leads to the following system of equations:

$$\mathbb{K} \mathbb{T} = \mathbb{F}, \quad (4)$$

where \mathbb{K} is the global stiffness matrix, \mathbb{T} is the global nodal temperature vector, and \mathbb{F} represents the global nodal force vector. As usual, \mathbb{K} is assembled from the element stiffness matrices \mathbf{K}^e ,

$$\mathbf{K}^e = \int_{\Omega_e} \left(\mathbb{B}^e(\mathbf{X}) \mathcal{K}(\mathbf{X}) \mathbb{B}^e(\mathbf{X}) + \mathbb{N}^e(\mathbf{X}) \tilde{h} \mathbb{W}^e(\mathbf{X}) \right) d\Omega + \sum_{j=1}^{n_{ch}} \int_{\Gamma_f^{(j)} \cap \Omega_e} \mathbb{B}^e(\mathbf{X}) \mathbf{t}^{(j)} \dot{m}^{(j)} c_f \mathbb{W}^e(\mathbf{X}) d\Gamma, \quad (5)$$

where the prime symbol $(\cdot)'$ represents the transpose of (\cdot) , \mathbb{W}^e is the SUPG weighting function defined in (B.7), $\mathbb{N}^e = [\mathbf{N}(\mathbf{X}) \quad \Psi(\mathbf{X})]$

is the element shape function, and $\mathbb{B}^e = [\mathbf{B}_N(\mathbf{X}) \quad \mathbf{B}_\psi(\mathbf{X})]$ is the derivative of the shape function. For elements which are not intersected by microchannels, $\Psi = 0$ and $\mathbf{B}_\psi = 0$.

Similarly, the global nodal force vector \mathbb{F} in (4) is assembled from the element nodal force vector \mathbf{F}^e ,

$$\mathbf{F}^e = \int_{\Omega_e} \mathbb{W}^e(\mathbf{X}) \left(f(\mathbf{X}) + \tilde{h} T_{amb} \right) d\Omega + \int_{\Gamma_e \cap \Gamma_q} \mathbb{N}^e(\mathbf{X}) q_p''(\mathbf{X}) d\Gamma. \quad (6)$$

Standard isoparametric FEM with Gauss quadrature is used herein to evaluate the integrals that define element stiffness matrices and load vectors. However, this requires special care when calculating over the enriched elements due to the discontinuity of the interpolation, as the enriched element Ω_e must be divided into several integration elements $\Omega_e^{(i)}$. The details of evaluating (5) and (6) are explained in [26,42].

2.3. Dimensionally reduced hydraulic model for microvascular materials

In this study, we assume that the coolant flow is fully developed, steady-state, and laminar. Using fully developed Hagen-Poiseuille flow [44], we can assume that the flow rate scales linearly with the pressure drop. Nodal pressures $P_{inlet}^{(j)}$ and $P_{outlet}^{(j)}$ of microchannel j , and the contribution of its mass flow rate $S_{inlet}^{(j)}$ and $S_{outlet}^{(j)}$ are coupled as follows:

$$g^{(j)} \begin{bmatrix} 1 & -1 \\ -1 & 1 \end{bmatrix} \begin{Bmatrix} P_{inlet}^{(j)} \\ P_{outlet}^{(j)} \end{Bmatrix} = \begin{Bmatrix} S_{inlet}^{(j)} \\ S_{outlet}^{(j)} \end{Bmatrix}, \quad (7)$$

where $g = \frac{Cv^4}{\mu L}$, L , and v are microchannel conductance, length, and fluid kinematic viscosity, respectively. For a square cross-section, $C = 1/28.46$, and for a circular cross-section $C = \pi/128$ [44,45], and D is the microchannel diameter and width for circular and square cross-sections, respectively. The underlying assumptions for this model are summarized in [Appendix A](#).

The assembly form of Eq. (7) can be written as

$$\mathbb{G} \mathbf{P} = \mathbf{S}, \quad (8)$$

where \mathbb{G} is the assembled conductance matrix of dimension: $(n_{end \ points} \times n_{end \ points})$, where \mathbf{P} and \mathbf{S} are the column vectors of nodal pressures and mass flow rates, respectively. From (8), the pressure drop (ΔP) in each microchannel can be obtained, where the mass flow rates of each microchannel can be computed as follows:

$$\dot{m}^{(j)} = g^{(j)} | \Delta P^{(j)} |. \quad (9)$$

3. Gradient-based HyTopS optimization method

In this section, the goal is to develop a HyTopS optimization scheme that has the ability to change the topology of the network by creating/removing microchannels during the shape optimization process. This task has been carried out by introducing a new set of design parameters which act analogous to the penalization factor of defined previously (SIMP) method. Three different types of design parameters are defined: (1) the location of the control/end points of the microchannels; (2) diameters of the microchannels; and (3) weighting parameters (α_i).

The first two design parameters are responsible for shape and size optimization of the network, and their full sensitivity analysis are evaluated and verified in [4,22]. The newly introduced design parameter (α_i) enables the optimizer to create/remove the microchannels and augment the topology of the network. $\alpha_i \in [0, 1]$ can be viewed as a weighting of the effective diameter given by:

$$D_{\text{eff}}^{(i)} = \alpha_i^\eta D_i, \quad (10)$$

where η is a penalization power analogous to the penalization parameter defined in the SIMP method, and D_i is the initial diameter of the respective microchannel. A similar idea was suggested by Norato et al. [46] for topology optimization of structures made from discrete elements. The penalization power typically needs to be greater than or equal to 3 as suggested by prior studies [34]. The distributions of the normalized effective diameter versus the weighting parameter α for different penalization powers are shown in Fig. 2.

The mass flow rate of a particular microchannel will become quite small when the effective diameter of that microchannel is below a certain value. Such microchannels will have a negligible effect on the value of the objective function introduced in Section 3.1. Therefore, we remove microchannels with mass flow rates lower than a defined threshold and retain microchannels when mass flow rates are above the threshold. A threshold is chosen such that the effect of removing microchannels on (i) the objective value, (ii) mass flow rates of other microchannels, and (iii) nodal pressures of the network are negligible. This threshold selection procedure is further discussed in Appendix C. Topological change is of particular interest when strict constraints are imposed on the microchannel volume fraction or pressure drop. In this situation, the optimizer has flexibility in satisfying such constraints by creating or removing the microchannels, as detailed in Section 5.

3.1. Sensitivity analysis and adjoint method

A general finite-element-based optimization problem can be formulated as:

$$\begin{aligned} & \min_{\mathbf{d}} \theta(\mathbb{T}(\mathbf{X}(\mathbf{d}), \mathbf{d}), \mathbf{X}(\mathbf{d}), \mathbf{d}), \\ & \text{such that: } d_i^{lb} \leq d_i \leq d_i^{ub}, \\ & \quad g_j(\mathbb{T}(\mathbf{X}(\mathbf{d}), \mathbf{d}), \mathbf{X}(\mathbf{d}), \mathbf{d}) \leq 0, \\ & \text{with } j = 1, 2, \dots, l, \\ & \text{and } \mathbb{K}(\mathbf{X}(\mathbf{d}))\mathbb{T}(\mathbf{X}(\mathbf{d}), \mathbf{d}) = \mathbb{F}(\mathbf{X}(\mathbf{d})), \end{aligned} \quad (11)$$

where θ denotes the cost or objective function to minimize, g_j is the constraint function, \mathbf{X} represents the nodal coordinates of the mesh and, \mathbf{d} is the design parameter vector defined as $\mathbf{d} = \{d_1^{(t_1)}, \dots, d_{nd_1}^{(t_1)}, d_1^{(t_2)}, \dots, d_{nd_2}^{(t_2)}, d_1^{(t_3)}, \dots, d_{nd_3}^{(t_3)}\}$, in which, the superscript indicates the design parameter's type (t_1 : control points, t_2 : diameters, t_3 : weighting parameters), and the subscript represents the design parameter's index. Note that \mathbf{X} , \mathbb{K} , \mathbb{T} , and \mathbb{F} are all functions of \mathbf{d} .

To carry out a gradient-based optimization, a sensitivity analysis is required to calculate the objective and constraint functions' gradients with respect to the design variables. The sensitivity analysis of the objective function and constraints with respect to the

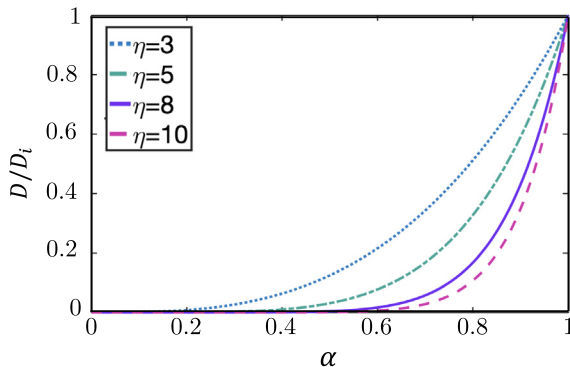


Fig. 2. Normalized effective diameter (D) versus weighting parameter (α).

control points and diameters are previously derived in [4,22] using the adjoint method for IGFEM developed in [26]. In the current study, the sensitivity analysis of the objective function with respect to the newly introduced design parameter α is conducted by using an analytical discrete derivatives method based on the direct and adjoint approaches.

The sensitivity of the objective function (11) is as follows:

$$\frac{d\theta}{d\mathbf{d}_i} = \left(\frac{\partial\theta}{\partial\mathbb{T}}\right)' \mathbb{T}_i^* + \left(\frac{\partial\theta}{\partial\mathbf{X}}\right)' \mathbb{V}_i + \frac{\partial\theta}{\partial d_i}, \quad (12)$$

where \mathbb{T}_i^* is the shape material derivative $\mathbb{T}_i^* = (\partial\mathbb{T}/\partial\mathbf{X})\mathbb{V}_i + \partial\mathbb{T}/\partial d_i$ and \mathbb{V}_i denotes the shape velocity field defined by $\mathbb{V}_i(\mathbf{X}, d_i) = \partial\mathbf{X}/\partial d_i$. Note that the shape velocity field \mathbb{V}_i is zero for the design parameters α_i , i.e., $\mathbb{V}_i(\mathbf{X}, \alpha_i) = 0$. Therefore, the sensitivity of the objective function with respect to α_i can be written as

$$\frac{d\theta}{d\alpha_i} = \left(\frac{\partial\theta}{\partial\mathbb{T}}\right)' \frac{\partial\mathbb{T}}{\partial\alpha_i} + \frac{\partial\theta}{\partial\alpha_i}, \quad (13)$$

where $\partial\theta/\partial\mathbb{T}$ and $\partial\theta/\partial\alpha_i$ are explicitly evaluated and the shape material derivative $\partial\mathbb{T}/\partial\alpha_i$ is computed in the pseudo analysis that will be discussed later.

The goal is to minimize the maximum temperature, but the maximum temperature function (T_{max}) is not differentiable. To overcome this issue, the maximum function is often approximated by a differentiable alternative such as the Kreisselmeier-Steinhauser function or the p -norm [47–49].

In this study, we substitute T_{max} with the temperature p -norm $\|T\|_p = (\int_{\Omega} T^p d\Omega)^{1/p}$ where $|\Omega|$ is the area of the domain. Note that $\lim_{p \rightarrow \infty} \|T\|_p = T_{\text{max}}$.

Regarding the value of p , we adopt $p = 8$ based on our previous observation in [4]. Therefore, the objective function of this study is defined as:

$$\theta = (\|T\|_p)^p = \int_{\Omega} T^p d\Omega = \int_{\Omega} (\mathbb{N}\mathbb{T})^p d\Omega. \quad (14)$$

A 16-point Gauss–Dunavant quadrature [50] is needed to exactly compute the integration of (14) over a triangular element with $p = 8$.

Note that the objective function (14) is not explicitly a function of α_i , i.e., $\partial\theta/\partial\alpha_i = 0$. Following (13), and taking the derivative of the objective function (14) with respect to α_i , results in:

$$\frac{d\theta}{d\alpha_i} = \int_{\Omega} \left[p(\mathbb{N}\mathbb{T})^{p-1} \mathbb{N} \frac{\partial\mathbb{T}}{\partial\alpha_i} \right] d\Omega. \quad (15)$$

In the following pseudo analysis, the discrete linear system of equations relevant to the primal (4) problem is differentiated with respect to each one of the design variables α_i , leading to a series of pseudo problems:

$$\mathbb{K} \frac{\partial\mathbb{T}}{\partial\alpha_i} = \mathbb{F}_{\text{pseudo}}^i, \quad (16)$$

where

$$\mathbb{F}_{\text{pseudo}}^i = -\frac{\partial\mathbb{K}}{\partial\alpha_i} \mathbb{T} + \frac{\partial\mathbb{F}}{\partial\alpha_i}. \quad (17)$$

The terms of (17) can be computed by assembling the element quantities $\partial\mathbb{K}^e/\partial\alpha_i$ and $\partial\mathbb{F}^e/\partial\alpha_i$:

$$\begin{aligned} \frac{\partial\mathbb{K}^e}{\partial\alpha_i} &= \int_{\Omega_e} \left[\frac{\partial\mathbb{B}^e}{\partial\alpha_i} \mathbb{K} \mathbb{B}^e + \mathbb{B}^e \frac{\partial\mathbb{K}}{\partial\alpha_i} \mathbb{B}^e + \mathbb{B}^e \mathbb{K} \frac{\partial\mathbb{B}^e}{\partial\alpha_i} + \frac{\partial\mathbb{N}^e}{\partial\alpha_i} \tilde{h} \mathbb{W}^e + \mathbb{N}^e \tilde{h} \frac{\partial\mathbb{W}^e}{\partial\alpha_i} \right] d\Omega \\ &+ \sum_{j=1}^{n_{ch}} \int_{\Gamma_j^{(j)} \cap \Omega_e} \left[\mathbb{B}^e \mathbf{t}^{(j)} \dot{m}^{(j)} c_f \frac{\partial\mathbb{W}^e}{\partial\alpha_i} + \frac{\partial\mathbb{B}^e}{\partial\alpha_i} \mathbf{t}^{(j)} \dot{m}^{(j)} c_f \mathbb{W}^e \right. \\ &+ \left. \mathbb{B}^e \mathbf{t}^{(j)} \frac{\partial\dot{m}^{(j)}}{\partial\alpha_i} c_f \mathbb{W}^e + \mathbb{B}^e \mathbf{t}^{(j)} \dot{m}^{(j)} c_f \frac{\partial\mathbb{W}^e}{\partial\alpha_i} \right] d\Gamma, \end{aligned} \quad (18)$$

and

$$\begin{aligned} \frac{\partial \mathbf{F}^e}{\partial \alpha_i} &= \int_{\Omega_e} \left(\frac{\partial \mathbb{W}^e}{\partial \alpha_i} (f + \tilde{h}T_{amb}) + \mathbb{W}^e \frac{\partial f}{\partial \alpha_i} \right) d\Omega \\ &+ \int_{\Gamma_e \cap \Gamma_q} \left(\frac{\partial \mathbb{N}^e}{\partial \alpha_i} q_p'' + \mathbb{N}^e \frac{\partial q_p''}{\partial \alpha_i} \right) d\Gamma. \end{aligned} \quad (19)$$

Note that $\mathbb{N}^e, \mathbb{B}^e, \mathbf{t}^{(j)}, q_p'', f$, and \mathcal{K} are not a function of α , i.e., $\partial \mathbb{N}^e / \partial \alpha_i, \partial \mathbb{B}^e / \partial \alpha_i, \partial \mathbf{t}^{(j)} / \partial \alpha_i, \partial q_p'' / \partial \alpha_i, \partial f / \partial \alpha_i$, and $\partial \mathcal{K} / \partial \alpha_i$ are all equal to zero. Furthermore, as explained in Appendix D, $\partial \mathbb{W}^e / \partial \alpha_i$ is zero. Therefore, (18) and (19) reduce to:

$$\frac{\partial \mathbf{K}^e}{\partial \alpha_i} = \sum_{j=1}^{n_{ch}} \int_{\Gamma_j^{(j)} \cap \Omega_e} \mathbb{B}^e \mathbf{t}^{(j)} \frac{\partial \dot{m}^{(j)}}{\partial \alpha_i} c_f \mathbb{W}^e d\Gamma, \quad (20)$$

and

$$\frac{\partial \mathbf{F}^e}{\partial \alpha_i} = 0, \quad (21)$$

where $\partial \dot{m}^{(j)} / \partial \alpha_i$ is given by:

$$\frac{\partial \dot{m}^{(j)}}{\partial \alpha_i} = \frac{\partial \mathbf{g}^{(j)}}{\partial \alpha_i} \left(P_{inlet}^{(j)} - P_{outlet}^{(j)} \right) + \mathbf{g}^{(j)} \text{sign} \left(P_{inlet}^{(j)} - P_{outlet}^{(j)} \right) \left(\frac{\partial P_{inlet}^{(j)}}{\partial \alpha_i} - \frac{\partial P_{outlet}^{(j)}}{\partial \alpha_i} \right), \quad (22)$$

and using (8), $\partial \mathbf{P} / \partial \alpha_i$ is as follows:

$$\frac{\partial \mathbf{P}}{\partial \alpha_i} = \mathbb{G}^{-1} \left(\frac{\partial \mathbf{S}}{\partial \alpha_i} - \frac{\partial \mathbb{G}}{\partial \alpha_i} \mathbf{P} \right). \quad (23)$$

Note that \mathbf{S} is not a function of α_i , i.e., $\partial \mathbf{S} / \partial \alpha_i = 0$. In addition, $\partial \mathbb{G} / \partial \alpha_i$ can be explicitly evaluated.

In summary, in the direct differentiation sensitivity analysis for each parameter α_i , we evaluate the pseudo load \mathbb{F}_{pseudo}^i and solve (16) to evaluate $\partial \mathbb{T} / \partial \alpha_i$. Having $\partial \mathbb{T} / \partial \alpha_i$, we compute the sensitivity (13) for the objective function. A similar approach can be used to find the gradient of constraints with respect to the design parameters.

Alternatively, the sensitivity of the objective function can be obtained using the adjoint method by eliminating $\partial \mathbb{T} / \partial \alpha_i$ from (13). The number of operations in the direct method is $O(n_d \times n_{dof}^2)$, and by implementing the adjoint method, the number of operations is further reduced and becomes independent of the design variables, i.e., $O(n_d)$. Considering an arbitrary multiplier λ , the adjoint vector, the sensitivity (13) can be re-written as¹:

$$\begin{aligned} \frac{d\theta}{d\alpha_i} &= \left(\frac{\partial \theta}{\partial \mathbb{T}} \right)' \frac{\partial \mathbb{T}}{\partial \alpha_i} + \frac{\partial \theta}{\partial \alpha_i} + \lambda' \left(-\mathbb{K} \frac{\partial \mathbb{T}}{\partial \alpha_i} + \mathbb{F}_{pseudo} \right) \\ &= \left(\left(\frac{\partial \theta}{\partial \mathbb{T}} \right)' - \lambda' \mathbb{K} \right) \left(\frac{\partial \mathbb{T}}{\partial \alpha_i} \right) + \frac{\partial \theta}{\partial \alpha_i} + \lambda' \mathbb{F}_{pseudo}. \end{aligned} \quad (24)$$

Based on the definition of the objective function in (14), the objective function θ is not explicitly a function of α , i.e., $\partial \theta / \partial \alpha_i$ is zero. Since the adjoint response λ is an arbitrary constant, we can set it in such a way that makes the coefficient of $\partial \mathbb{T} / \partial \alpha_i$ zero, thus we have:

$$\mathbb{K}' \lambda = \frac{\partial \theta}{\partial \mathbb{T}}, \quad (25)$$

and

$$\frac{d\theta}{d\alpha_i} = \lambda' \mathbb{F}_{pseudo}. \quad (26)$$

¹ Based on (16), $\left(-\mathbb{K} \frac{\partial \mathbb{T}}{\partial \alpha_i} + \mathbb{F}_{pseudo} \right)$ is zero, so we can add it to the right hand side of (13).

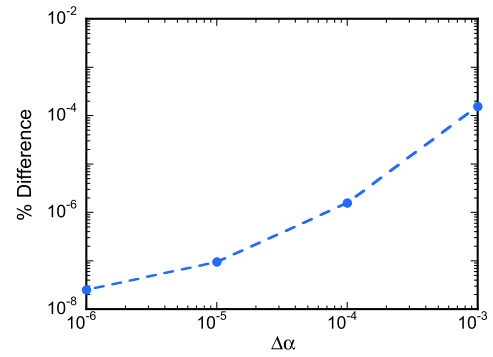


Fig. 3. Percent difference in the objective function gradient from the adjoint method and central finite difference with respect to α .

Note that \mathbb{K} in (25) is not symmetric due to the convection term. The pseudo problem (16) needs to be solved n_d times, while the adjoint problem (25) only requires solving once. By substituting λ obtained from (25) into (26), the gradient of the objective function with respect to α_i can be determined.

As shown in Fig. 3, the percent difference between the gradients of the objective function with respect to α obtained from central finite difference and adjoint method is practically negligible. It can be seen that as $\Delta\alpha$ becomes less than 10^{-4} , the percent difference converges to less than $10^{-6}\%$.

4. Validation of method

The IGFEM solver has been previously verified in [14,27,38,51]. Shape sensitivity analysis for structural and thermal problems in the IGFEM framework has also been verified in [26], and its application to microvascular materials validated in [4,22,24], verified with the analytical solution in [42] and also with ANSYS FLUENT in [4,52]. In this section, the new IGFEM-based HyTopS optimization method is experimentally validated using a recent 3D-printing technique to create interconnected microvasculature in fiber-composites [53].

4.1. Optimization problem

The problem is graphically depicted in Fig. 4 where the simulation parameters and material properties are listed in Table 1. A carbon-fiber/epoxy-matrix composite panel of size $L_x = 150$ mm, $L_y = 200$ mm, and a thickness of 3.0 mm is subjected to a uniform

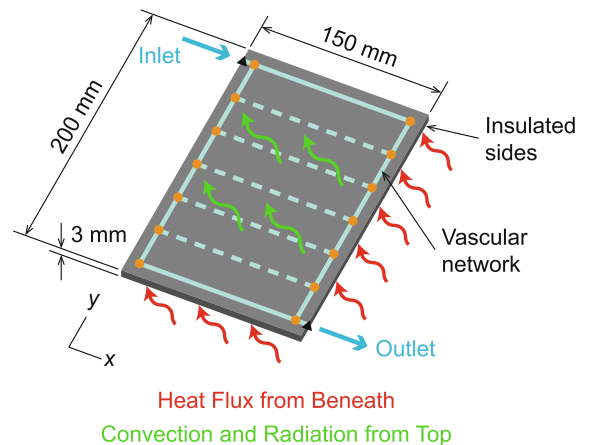


Fig. 4. Schematic of problem setup, boundary conditions, and design parameters.

Table 1
Simulation parameters, coolant and material thermal properties.

Dimension in x direction, L_x (mm)	150
Dimension in y direction, L_y (mm)	200
Thickness, t (mm)	3
Ambient Temperature, T_{amb} ($^{\circ}\text{C}$)	23
Convection coefficient, h_{conv} ($\text{Wm}^{-2} \text{K}^{-1}$)	18.1
Emissivity, ϵ	0.95
Panel thermal conductivity, κ_p ($\text{Wm}^{-1} \text{K}^{-1}$)	2.07
Coolant conductivity, κ_c ($\text{Wm}^{-1} \text{K}^{-1}$)	0.419
Coolant density, ρ_c (kgm^{-3})	1065
Coolant heat capacity, c_f ($\text{Jkg}^{-1} \text{K}^{-1}$)	3494
Coolant inlet flow rate, \dot{V}_{in} (mL min^{-1})	40
Coolant inlet temperature, T_{in} ($^{\circ}\text{C}$)	23.1

thermal heat flux of 500 Wm^{-2} from the bottom surface. The top surface is free to have radiation and convection heat transfer with the ambient environment, but the sides are insulated. The thermal conductivity of the panel is $2.07 \text{ Wm}^{-1} \text{K}^{-1}$, which represents a carbon composite with a fiber volume fraction of 46% [3,5]. Moreover, it is assumed that the composite reinforcement is balanced and has isotropic in-plane thermal conductivity. The microchannel cross-sections are assumed to be circular with a diameter of $500 \mu\text{m}$. The coolant is a 50:50 water:ethylene glycol mixture, which is typical for batteries [21] and fuel cells [54], and enters the network at a temperature of $23.1 \text{ }^{\circ}\text{C}$ and volumetric flow rate of 40 mL min^{-1} from the top left inlet. The coolant exits from the bottom right outlet at a zero-reference pressure. The thermal conductivity and heat capacity of the liquid is substantially higher than air; therefore, it provides enhanced cooling performance.

Three design parameters are considered in this problem. First, the location of control points indicated by the solid circles in Fig. 4, where the bounding boxes are chosen as $0.005 \leq x \leq 0.145$ and $0.005 \leq y \leq 0.195$ (in m). Note that the inlet and outlet control points (black triangles) are fixed. The other two design parameters are defined for the interior microchannels indicated by the dashed lines in Fig. 4. One is the diameter which can vary between 100 and $500 \mu\text{m}$, and the other continuous diameter weighting parameter (α_i) that varies between 0 and 1. For this problem, the mass flow-rate threshold ($\dot{m}c_f$) below which microchannels are removed is set to $10^{-3} \text{ Js}^{-1} \text{ K}^{-1}$, and the penalization power η is 8. The minimum and maximum number of branches that the network can obtain during the optimization process also needs to be specified. From a computational point of view, there is no limitation on the number of branches within the HyTopS optimization framework. However, from a fabrication

viewpoint, the number of branches will depend on various factors such as manufacturing constraints and intended operating conditions. In this example, we set the minimum and the maximum number of branches to 1 and 6, respectively. The objective function for this problem is to minimize the temperature p -norm of the panel with $p = 8$, and additional geometrical constraints described in [4] that are imposed to ensure manufacturability of the optimum design.

The optimization problem is solved and the results are summarized in Fig. 5. The initial (reference) and optimal microvascular network designs are shown in Fig. 5(a and b). It can be seen that the optimizer created three additional microchannels, thus changing the number of branches from 3 to the maximum allowed 6. The temperature distributions of the reference and optimum designs are shown in Fig. 5(c and d). The maximum panel temperature is reduced from $38.7 \text{ }^{\circ}\text{C}$ in the initial configuration to $32.3 \text{ }^{\circ}\text{C}$ in the optimum design.

One of the challenges in determining the optimum value of the objective function is the existence of multiple local optima due to the non-convex nature of the gradient-based HyTopS optimization scheme. To address this issue, we created fifty, distinct initial guesses as depicted in Fig. 6(a). These designs are produced by changing the location of control points, diameters of the microchannels, and the number of branches. Most of these cases (88%) converge to the optimal, maximum temperature of $32.6 \pm 0.3 \text{ }^{\circ}\text{C}$. Seven interesting initial designs out of the 50 cases are selected, and their history plot, initial and optimum network configurations, and associated temperature distributions are shown in Fig. 6(b). It is worth noting that the optimization process starting from 1- to 6- parallel horizontal branches and a 3-branch parallel vertical network results in almost similar optimum designs and fairly close objective values. This observation will be discussed in more detail in Section 5.1.

4.2. Experimental samples

Microvascular networks based on reference and optimal designs are created in a carbon-fiber/epoxy-matrix composite using an established vascularization (VaSC) process [2] in conjunction with a recent 3D printing technique to construct sacrificial polymer network templates with branches/interconnects [53]. Fig. 7(a) shows a printed optimized network template placed atop a carbon-fiber fabric (Toray T300 3 K plain weave) with a zoomed inset of an interconnection. The printed vascular templates were solvent-bonded using acetone to the woven carbon-fiber ply that was then placed in the mid-plane of a symmetric, 12 layer stack and the composite preform was infused with epoxy resin using vacuum assisted resin transfer molding (VARTM). After 24 h at

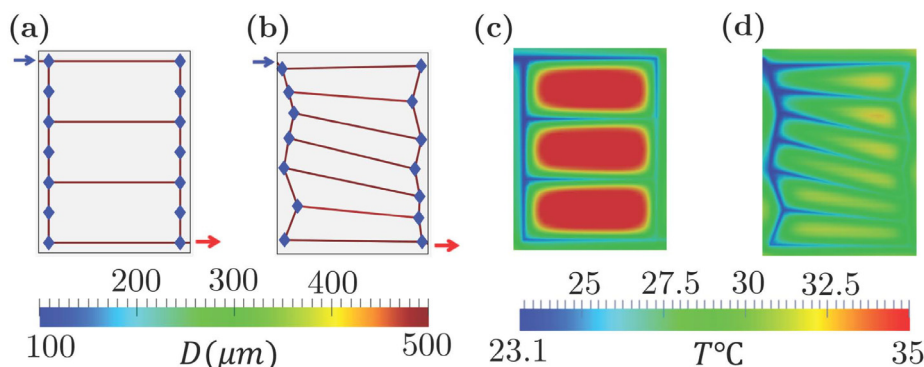


Fig. 5. (a) Reference, and (b) optimal designs. (c) Temperature distribution corresponding to the reference, and (d) optimal designs. The optimizer creates three additional microchannels and reduces the maximum temperature from 38.7 to $32.3 \text{ }^{\circ}\text{C}$.

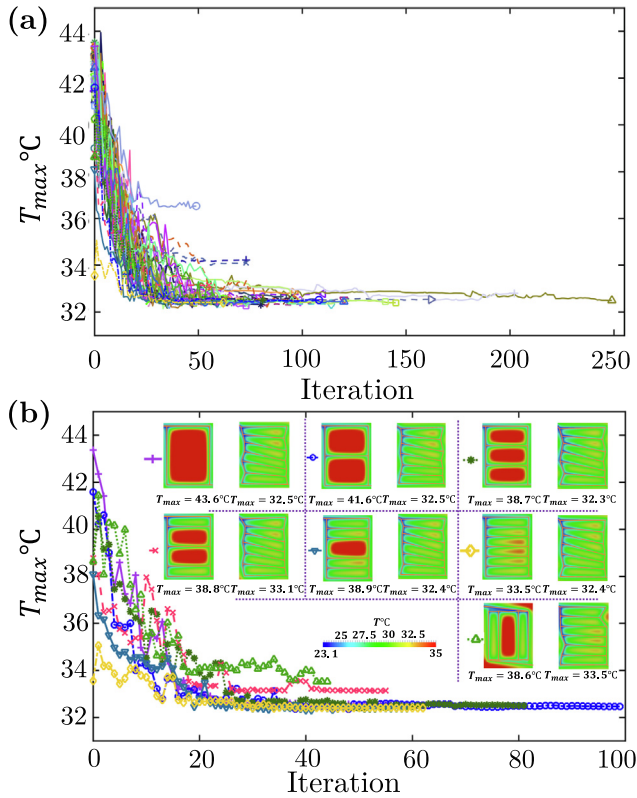


Fig. 6. (a) Evolution of the maximum temperature (T_{max}) during the HyTopS optimization starting from 50 random initial configurations, and (b) T_{max} history plot, initial/optimum network designs, and associated temperature distributions of seven interesting cases out of the 50 random configurations from part (a). More than 88% of the initial designs converge to the optimal, maximum temperature of 32.6 ± 0.3 °C.

room temperature, vacuum was released and the carbon-fiber composite was cured in a forced convection oven for 2 h at 121 °C followed by 2 h at 150 °C, resulting in a glass transition temperature of 143 °C measured by differential scanning calorimetry (DSC) [55]. After cure, the composite panels were cut to size ($\approx 150 \times 200$ mm) exposing the inlet/outlet cross-sections, and the sacrificial templates were subsequently removed using the VaSC process at 200 °C under ≈ 110 mTorr of vacuum for 12 h; resulting microchannel cross-sections were approximately 500 μ m in diameter as shown in Fig. 7(b). Holes were drilled (≈ 0.81 mm diameter) in the resulting inlet/outlet orifices in order to provide a tight fit of 20 gauge micro-nozzles for coolant delivery.

The average thickness of the composite panels was 2.96 ± 0.06 and 3.09 ± 0.03 mm, with fiber volume fractions of 46.9 ± 1.36 and $45.07 \pm 2.05\%$ [56], for reference and optimized networks respectively. An increase in composite thickness of approximately 30 μ m directly above the microchannels was measured by contact profilometry.

4.3. Thermal testing

A schematic of the active-cooling test setup is shown in Fig. 8. Vascular composites were adhered to a $150 \times 200 \times 6$ mm (width \times length \times thickness) copper plate using thermal grease and placed atop a polyimide film, resistive heater (Omega Part #: KH608/2) having the same areal dimensions. The sample assembly was insulated below by a balsa wood platform and on the sides by chloroprene rubber foam. Resistive heating was controlled by a programmable DC power supply (Tektronix Part #: PWS4602) under constant voltage. Input voltage (≈ 40 V) was determined for the prescribed heat flux of 500 W m^{-2} using Eq. (27) where q'' , V , R , and A_h denote areal heat flux, applied voltage, heater resistance (105 Ω), and heater area respectively:

$$q'' = V^2 / RA_h. \quad (27)$$

The top surface temperature of the vascular composite was recorded by an overhead mounted infrared (IR) camera (FLIR Model #: A655sc). Uniform temperature distribution of the vascular composite assembly under ambient and heated conditions was confirmed (Fig. 9). Additionally, thermocouples (Omega Part #: TMQSS-020U) were installed at the IR camera height to measure ambient temperature and also within the tubing near the inlet and outlet nozzles to measure fluid entry/exit temperature during the active-cooling experiments. Delivery of a 50:50 water:ethylene glycol coolant was achieved by inserting 20 gage micro-nozzles into the microchannel inlet/outlet, which were connecting via Luer fittings and silicone tubing (3 mm ID) to a peristaltic pump (Cole-Parmer Masterflex Item # EW-07522-30). The pump was calibrated (for each panel) before each test to ensure differences in setup/network flow resistance did not result in deviations greater than 2% from the prescribed flow rate of 40 mL/min.

Active-cooling experiments were performed by first heating the composite panel to a hot steady-state (HSS), which is defined by the average surface temperature remaining constant within the IR camera resolution (≈ 0.2 °C) for a 10 min time period. Once HSS is achieved, coolant is pumped at the prescribed flow rate until the cold steady-state (CSS) condition is reached (Fig. 10), defined by the same HSS temperature/time criteria. Mass flow rate is recorded throughout the entire cooling portion of the experiment

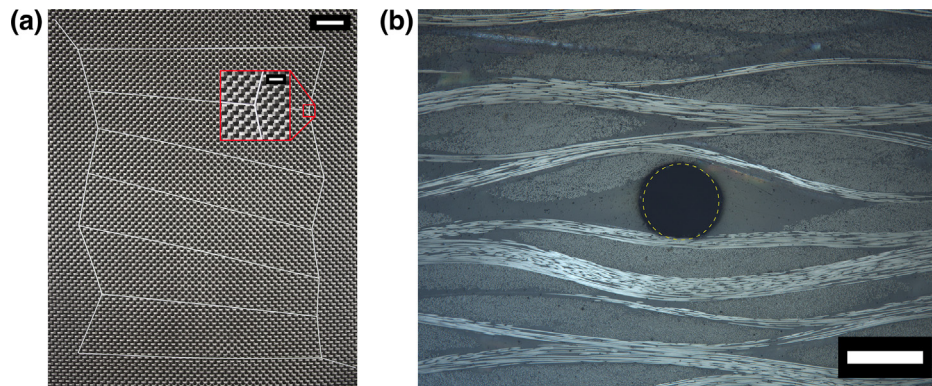


Fig. 7. (a) 3D printed, optimized network template atop a 3 K plain weave carbon-fiber fabric (scale bar = 15 mm) with zoomed inset of a triple junction (scale bar = 5 mm); (b) Optical microscope image of vascularized composite cross-section with exposed microchannel; dashed line represents 500 μ m diameter circle (scale bar = 500 μ m).

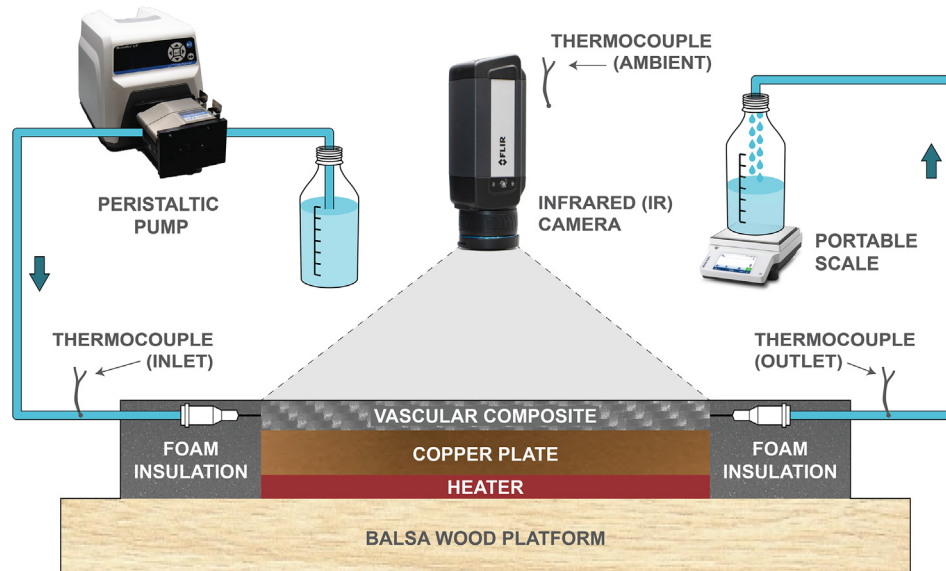


Fig. 8. Schematic of active-cooling experimental setup. Thermocouples were installed at the infrared (IR) camera height to measure ambient temperature, and within the tubing near the inlet and outlet nozzles to measure the coolant entry and exit temperature.

by weighing the outlet fluid and reporting the slope of the mass versus time relationship from a linear regression analysis. Volumetric flow rates, i.e., mass flow rates divided by coolant density, were 40.62 and 39.45 mLmin⁻¹ with an $R^2 = 1.0$ for the reference and optimum panels, respectively.

4.4. Experimental results and discussion

Fig. 11 compares the CSS temperature distributions of the reference and optimized networks. The maximum temperature obtained from the IGFEM simulations, ANSYS FLUENT, and experiments, respectively, are 38.7, 38.4, and 35.1 °C for the reference design, and 32.3, 33.1, and 33.2 °C for the optimum design. The absolute value of the average nodal temperature difference between the experiments and IGFEM thermal solver are 3.2 and 2.7 °C for the reference and optimum designs, respectively.

There are several sources that may have led to the discrepancy between the temperature distributions obtained from the simulations and experiments. First and foremost, the IGFEM thermal solver is a reduced order model based on several simplifying assumptions, discussed in detail in [Appendix A](#). Also, since the numerical model is two-dimensional, the simulated temperature distribution is from the middle of the panel at the vascular network centerline, while the experimental measurements are obtained from the top surface of the panel. The perfectly insulated boundary conditions and applied heat flux are only approximated in the experimental setup. Moreover, the homogenized heat transfer properties assumed for the carbon-fiber epoxy-matrix composite does not accurately capture local material heterogeneity, i.e. matrix pockets, surrounding the micro-channels as shown [Fig. 7](#) (b). Finally, with respect to the vascular network construction via 3D printing ([Fig. 7](#)), it is quite challenging to fabricate completely smooth, circular cross-sections and form perfect interconnects [53]. Since viscous flow at this size-scale is highly dependent on microchannel geometry, we intend to perform a manufacturing sensitivity analysis in future studies.

4.5. Design quality assessment

We define several measures to compare the quality of the reference and the optimum designs for active-cooling: (i) maximum temperature; (ii) temperature uniformity; (iii) relative rate of cooling; and (iv) cooling efficiency.

The first criteria dictates that a lower maximum temperature indicates a higher quality design. The measured maximum surface temperature is reduced by a modest two degrees from 35.1 °C in the reference design to 33.2 °C for the optimum design, at their respective cold steady-states (CSS). However, this provides a somewhat limited measure since a single hot-spot in a predominately cool domain, could pollute overall quality assessment.

A more encompassing uniformity criteria (ii) states that a smaller variation from a lower average temperature for a prescribed region, represents better cooling. The optimized network outperforms the reference design not only in an average temperature reduction (33.4 to 31.5 °C), but also in terms of uniformity indicated by a smaller standard deviation (1.3 to 1.0 °C). Moreover, a

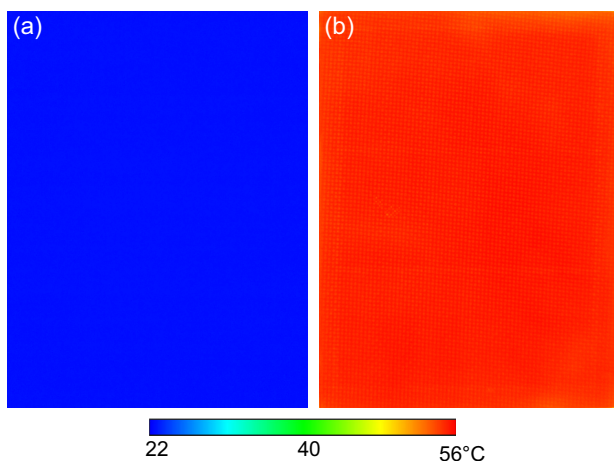


Fig. 9. Uniformity in composite surface temperature. (a) IR image of temperature distribution for composite panel with reference network at ambient conditions (average = 22.6 ± 0.1 °C); (b) IR image of temperature distribution for composite panel with reference network subjected to nominal heat flux of 500 Wm⁻² (average = 54.9 ± 0.5 °C).

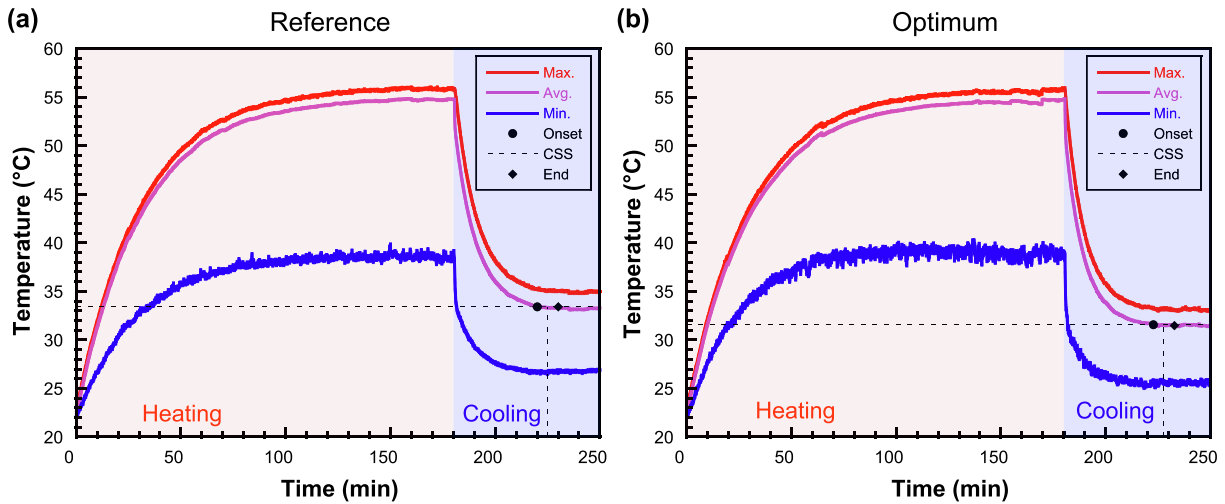


Fig. 10. IR camera surface temperature measurements versus time (a) Reference network (avg. temp. at CSS = 33.4 ± 1.3 °C); (b) Optimized network (avg. temp. at CSS = 31.5 ± 1.0 °C); dashed line indicates midpoint of cold steady state (CSS) region.

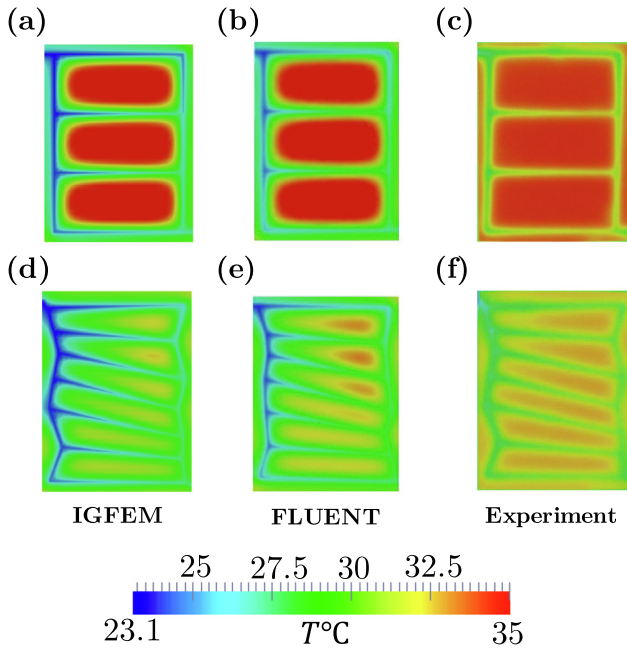


Fig. 11. Temperature distributions for the reference design from (a) IGFEM thermal solver, (b) ANSYS FLUENT, and (c) Experiment. Temperature distributions for the optimum design from (d) IGFEM, (e) FLUENT, and (f) Experiment.

Probability Density Function (PDF) is computed using the *ksdensity* function in MATLAB to further quantify temperature uniformity:

$$\hat{f}(T) = \frac{1}{nh} \sum_{j=1}^n K\left(\frac{T - T_j}{h}\right), \quad (28)$$

where n is the number of data points, h is the bandwidth, T is the temperature, and $K(\cdot)$ is the kernel smoothing function. As shown in Fig. 12, the peaks in the PDF distributions represent the most probable temperature in the domain, which are 34.4 and 32.5 °C for the reference and optimum designs, respectively. These peak temperatures are within a degree and follow the same decreasing trend as the computed average values. Analogous to the standard deviation, i.e. variation, the range of temperature in the PDF distributions can be regarded as a measure of uniformity. The range of temperatures is 8.8 and 8.1 °C for reference and optimum designs,

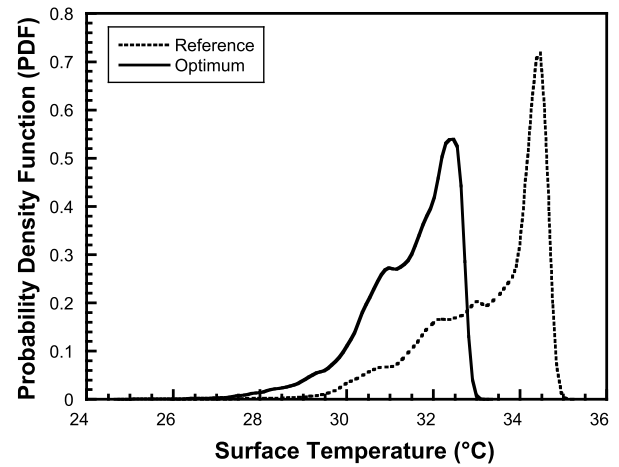


Fig. 12. Cold steady-state (CSS) surface temperature distributions for the reference and optimum designs represented by a probability density function (28). The optimum design has a lower peak (and average) temperature along with smaller temperature range (and standard deviation) in comparison to the reference design.

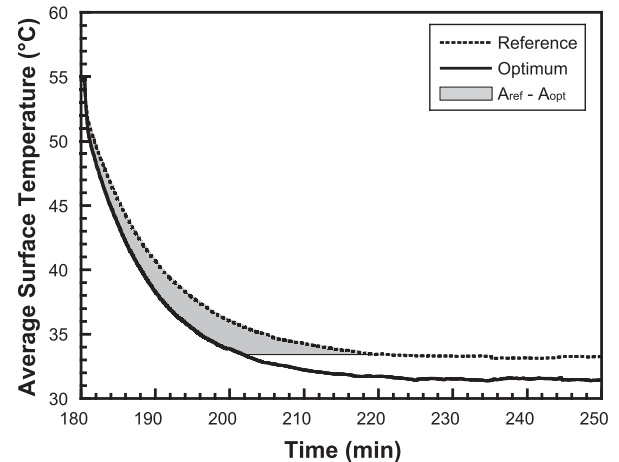


Fig. 13. Average surface temperature versus time for the active-cooling test segment. The shaded region is the difference in area of the reference and optimized panels bounded by the lowest common CSS temperature, which is used to calculate (29) the transient relative rate of cooling (RRC) metric.

respectively, further confirming the optimum network results in a more uniform temperature distribution.

While the simulations are time-independent and performed at steady-state, the experimental results provide additional information to assess the transient cooling performance. We define a new measure to compare the (iii) Relative Rate of Cooling (RRC) for the vascular composites as:

$$RRC = 1 - \frac{A_{opt}}{A_{ref}}, \quad (29)$$

Table 2
Parameters for the HyTopS versus shape optimization comparison.

Dimension in x direction, L_x (mm)	150
Dimension in y direction, L_y (mm)	200
Thickness, t (mm)	3
Panel thermal conductivity, κ_p ($Wm^{-1} K^{-1}$)	2.7
Coolant density, ρ_c (kgm^{-3})	1065
Coolant heat capacity, c_f ($Jkg^{-1} K^{-1}$)	3494
Coolant inlet flow rate, \dot{V}_{in} ($mL min^{-1}$)	28.2
Coolant inlet temperature, T_{in} ($^{\circ}C$)	27

where A_{opt} and A_{ref} are the respective optimized and reference areas under the average temperature versus time curves, from the start of cooling until reaching to the lowest common steady-state temperature. As shown in Fig. 13, the CSS temperature of the reference network governs for which the computed RRC is 31.3%. Hence, the optimum design is approximately 30% more effective in terms of the rate of cooling.

Lastly, we define (iv) cooling efficiency as the ratio of heat extracted by the coolant to the total heat flux applied [3]. This is calculated by Eq. (30), where q_e is the amount of heat extracted by the coolant, q_t is the total amount of applied heat to the composite:

$$\eta_c = \frac{q_e}{q_t} = \frac{\dot{m}c_p(T_{out} - T_{in})}{\int_{\Omega} f d\Omega}, \quad (30)$$

where T_{in} and T_{out} denote the measured inlet and outlet coolant temperatures.

The cooling efficiency at each respective CSS increased from 62.9% in the reference panel to 71.8% in the optimum design.

In summary, while the reference configuration was a well-informed, initial guess based on prior studies [3], the HyTopS opti-

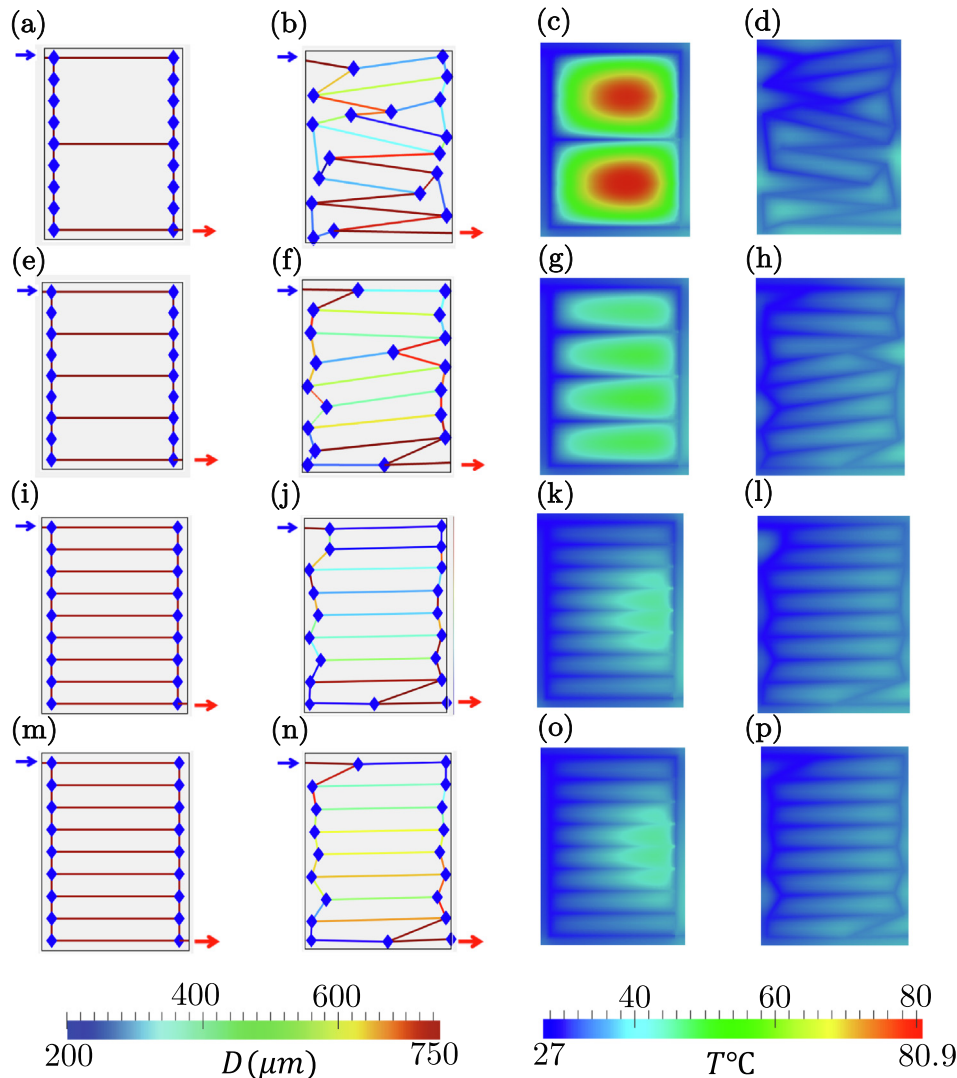


Fig. 14. HyTopS optimization: (a, e, i) initial/reference 2-, 4-, and 8-branch parallel networks, and (b, f, j) their optimal configurations; respective temperature distributions for reference (c, g, k) and optimal (d, h, l) configurations. Shape optimization of reference and optimal networks (m, n) and their respective temperature distributions (o, p).

mization method further enhanced the overall quality of the vascular cooling network in all measures.

5. Application examples

In this section, we solve two sets of application examples to demonstrate the advantages of the HyTopS optimization method over solely shape optimization approaches. In the first set, we show that in contrast to shape optimization, our HyTopS optimization scheme is capable of modifying the vascular topology during the optimization process. Therefore, the design space is not restricted to the topology of the initial guess. In the second set, we solve several examples to demonstrate the ability of HyTopS method to deal with strict constraints.

5.1. Topology versus shape optimization

One of the major limitations in gradient-based, shape optimization of microvascular materials is the inability to change the topology of the network during the optimization process. For instance, an initial design with n -branches of microchannels will undoubtedly end up with n -branches in the optimal network configuration. Thus choosing an appropriate topology for the initial design can be deemed an arduous task. Note that there is no way to figure out *a priori* which reference topology will lead to a better solution in terms of minimizing the objective function while satisfying the imposed constraints.

As explained earlier, the gradient-based HyTopS optimization method provides an efficient way to overcome topological evolution limitations. Under this approach, the optimizer determines at each iteration whether to create and/or remove microchannels in order to enhance the flexibility in minimizing the objective function while satisfying imposed constraints. Thus, in the HyTopS scheme, the initial network design is not a critical factor since the topology can be augmented throughout the optimization process.

To illustrate this capability, an application example for active-cooling of electric-vehicle battery packaging is presented. The simulation parameters, material properties, and working conditions are summarized in Table 2. Heat flux, coolant temperature, and coolant flow rate are identical to the operating conditions in the battery cooling panel of the Chevy Volt [21]. It is assumed that there is no heat loss due to convection or radiation from the surfaces of the panel. The microchannels' initial cross-sections are assumed to be square with height/width set to $750\ \mu\text{m}$. Similar to the example of Section 4.1, three types of design parameters are considered: microchannel control points; hydraulic diameters ranging from 200 to $750\ \mu\text{m}$, and interior microchannel weighting parameters. Additionally, as prescribed, the optimizer is allowed to modify the number of branches between 1 and 8.

As shown in Fig. 14(a, e, and i), the HyTopS optimization method is performed on initial 2-, 4-, and 8-branch parallel network designs, respectively. The objective function for this problem is the temperature p -norm of the domain ($p = 8$), where geometrical constraints are imposed to prevent self-crossing of the vasculature. Under the HyTopS optimization scheme, we expect to obtain a similar objective value in all three cases irrespective of the initial design topology, as shown in Fig. 15(a). The difference in the optimal objective values (8-norm of temperature) across these three cases is less than $0.59\ ^\circ\text{C}$.

Since the set of constraints are only geometric, it is expected the optimizer will increase the number of branches to minimize the temperature p -norm of the domain, as for the case shown in Fig. 14(b and f). Note that by increasing the number of microchannels, the respective share of the total flow rate in each channel

decreases. In such a scenario, the microchannels tend to shorten in order to maximize their cooling ability [4], which occurs for all of the optimal configurations in Fig. 14. This observation is explained by a simple energy balance for the heat transfer of a microchannel, which gives: $\dot{m}/L = \pi Dq''/(c_p(T_{out} - T_{in}))$. For a constant heat flux, a decrease in the mass flow rate through the channel requires a shorter length to produce an equivalent temperature change. Moreover, it is worth noting that HyTopS augments the diameters of the microchannels for the optimum solutions of Fig. 14(j and n) in order to produce more uniform flow rates within the middle microchannels; initial flow rates vary from 1.2 to $6.3\ \text{mLmin}^{-1}$ whereas the optimum flow rates vary from 2.2 to $3.5\ \text{mLmin}^{-1}$. As a result, the temperature distributions for the optimum solutions presented in Fig. 14(l and p) are more uniform in comparison to the initial designs (Fig. 14(k and o).

It is also worth mentioning that, although the optimal objective values in all of these cases are nearly identical to each other, their final vascular architectures are not the same. This is due to the very nature of optimization problems and schematically depicted in Fig. 16. In this figure, we assume that the curve represents the variation of the objective function versus a design parameter. It is conjectured that the optimization starts from three different initial points (A_1, B_1 , and C_1) and through paths A, B, and C, ends up at local minima A_2, B_2 , and C_2 , respectively. The local minima have equivalent objective function values but different values for the design parameter.

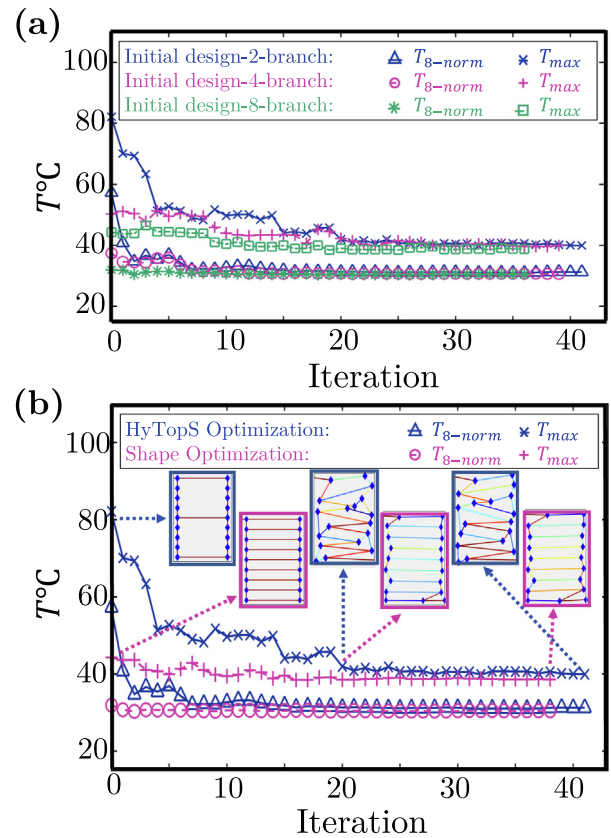


Fig. 15. (a) HyTopS history plots comparing objective function values (temperature 8-norm) and the maximum temperatures of three cases starting from 2-, 4-, and 8-branch parallel networks. (b) Comparison of the objective values and the maximum temperature evolutions starting from a 2-branch parallel network for the HyTopS optimization scheme and an 8-branch parallel network for the shape optimization method. The difference in objective values (temperature 8-norm) for the obtained optimum solutions is less than $0.59\ ^\circ\text{C}$.

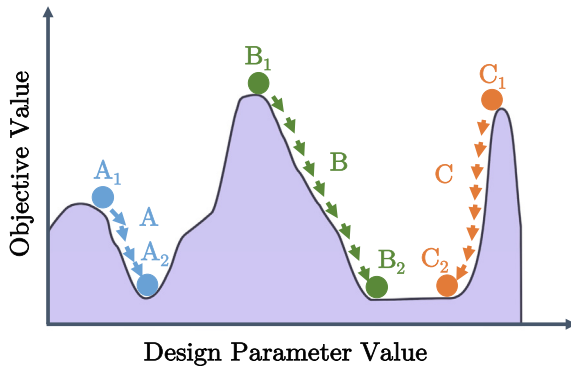


Fig. 16. Schematic illustrating local-minima pathways and how equal objective values can be obtained for different optimal configurations in a gradient-based optimization method.

We expect that performing shape optimization on the 8-branch parallel network design will result in a similar value obtained with the HyTopS objective function. The initial design, its optimal configuration, and respective temperature distributions are shown in Fig. 14(m-p), respectively. Fig. 15(b) shows the convergence history plots for the shape optimization scheme starting from the 8-branch parallel network and the HyTopS optimization method starting from the 2-branch parallel network. As expected, the difference between the optimal objective values in each case are neg-

ligible (i.e., within 2 percent). Thus the HyTopS optimization scheme, which allows topological changes of the microvascular network, effectively minimizes the objective function beginning from a primitive, initial design.

5.2. Constrained optimization

As described above, the HyTopS method is not limited to the topology of the initial design, and as a result, provides more flexibility to the optimizer. This flexibility is of particular interest when strict constraints are imposed to a problem. In such a scenario, the shape optimization scheme often fails to achieve an acceptable design. In this section, we investigate the ability of the HyTopS optimization method to circumvent strictly imposed constraints and achieve a favorable solution. Three different scenarios are presented, for which the simulation parameters, material properties, boundary conditions, objective functions, and geometrical constraints are similar to the example in Section 5.1. For all three examples within this section, the HyTopS optimizer is able to modify the number of branches from 1 to 8.

In the first example, the initial design is a parallel 2-branch network with a void volume fraction of 0.52%, where the void volume fraction is defined as the ratio of total microchannel volume over the total volume of the panel, i.e., $V_{void} = \frac{\sum_{i=1}^{n_{ch}} V^{(i)}}{V_{panel}}$.

The aim of the optimization is to minimize the temperature p -norm of the panel provided the void volume fraction remains less than 0.8%. Fig. 17(a-d) depicts the results of the gradient-based

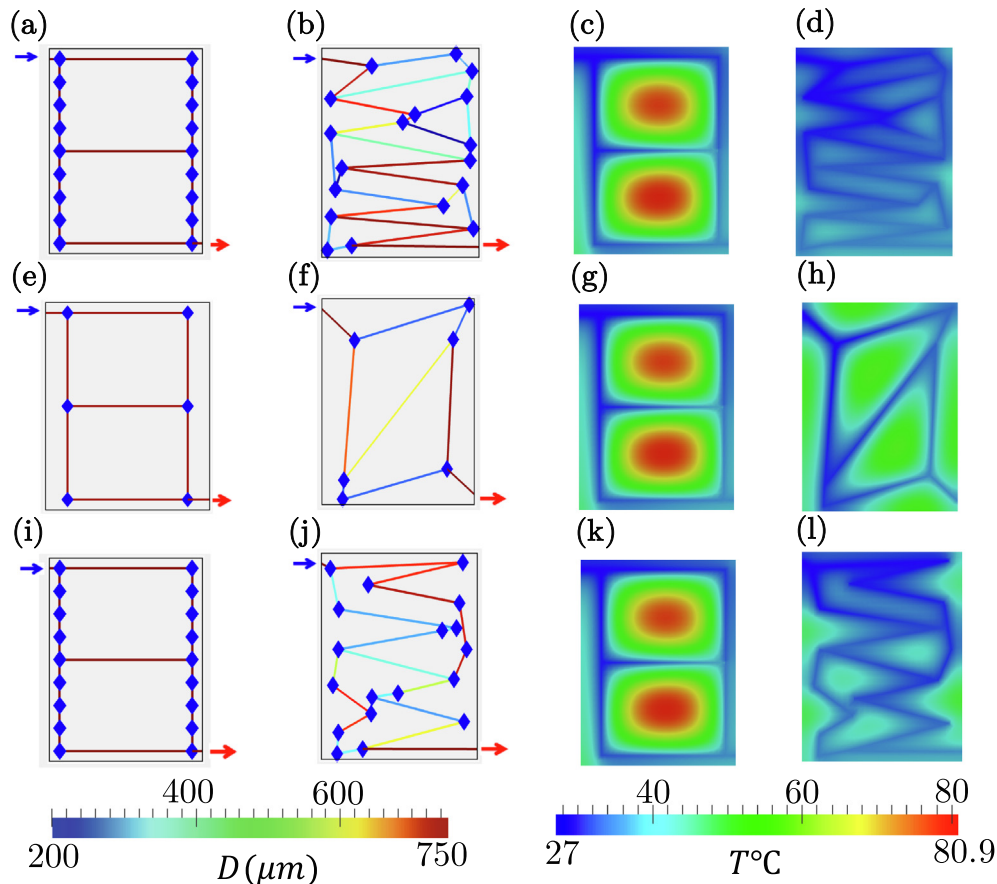


Fig. 17. HyTopS optimization: (a) initial, and (b) optimal designs and their respective temperature distributions (c, d). Shape optimization: *less control points* (e) initial and (f) optimal designs and their respective temperature distributions (g, h); *equal control points* (i) initial and (j) optimal designs and their respective temperature distributions (k, l). In all cases, the HyTopS optimization scheme outperforms the shape optimization method in minimizing the maximum temperature of the domain. Note: the optimization problem is subjected to a constraint on the microchannel volume fraction ($V_{void} \leq 0.8\%$).

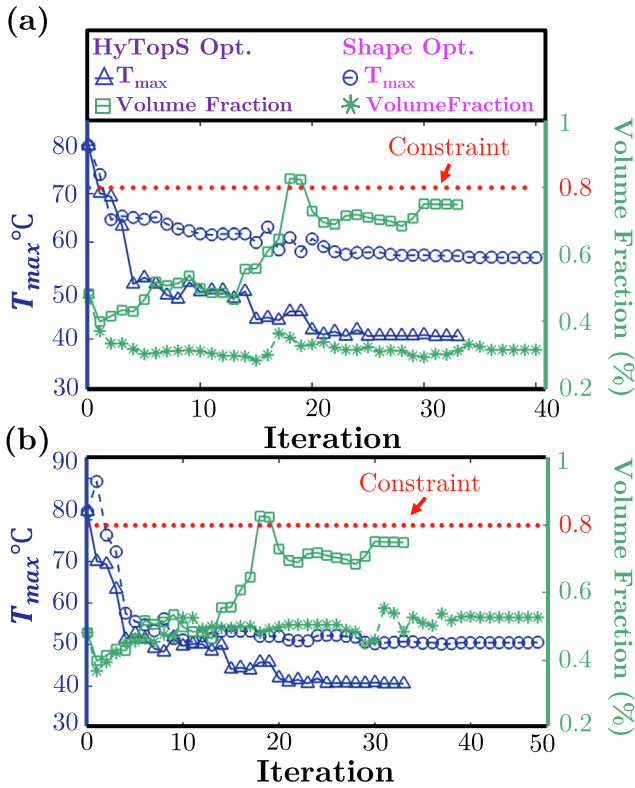


Fig. 18. (a) Comparison between the maximum temperature history plots for the HyTopS and shape optimization methods from the initial designs (Fig. 17(a, e)) with different number of control points. (b) Comparison between the maximum temperature history plots for the HyTopS and shape optimization methods from the initial designs (Fig. 17(a, i)) with equivalent number of control points. Note: the optimization problem is subjected to a constraint on the microchannel volume fraction ($V_{void} \leq 0.8\%$).

HyTopS optimization scheme. For comparison, the same objective is also carried out using the shape optimization method on an identical, initial 2-branch parallel network as shown in Fig. 17(e-h). As expected, the HyTopS optimizer takes advantage of

the latest microchannel additional/removal feature to significantly reduce the maximum panel temperature from 80.9 °C to 40.5 °C. In contrast, the maximum panel temperature for the shape optimization scheme is only reduced to 56.8 °C since the number of microchannels remains fixed (Fig. 18(a)).

In the preceding case, the number of control points for the initial design in the HyTopS optimization scheme was greater than the number of control points for the reference configuration in the shape optimization approach. In order to provide a more representative comparison, shape optimization is also conducted on an initial 2-branch parallel network with the same number of control points (Fig. 17(i-l)) as the initial design of the HyTopS optimization method (Fig. 17(a-d)). Summarized in Fig. 18(b), even when considering the same number of control points, the maximum panel temperature of the optimal configuration is still ten degrees higher at 50.5 °C.

To motivate the next example, we emphasize the importance of microvascular volume fraction, where many studies have been conducted to examine the effect of microchannels on the mechanical properties of the host composite. The effect of microchannels on tensile/compressive strength and stiffness [57–60], mode 1 and mode 2 fracture toughness [61], low-velocity impact response [62], and interlaminar shear strength [63] have been investigated. Results from these studies confirm that the mechanical properties are preserved when the microvascular volume fraction remains below 2% and when the fiber-reinforcement architecture (i.e., continuity of load-bearing plies) is not disrupted by incorporation of the microchannels [3]. Thus, all of the microchannel volume fractions considered in the examples of Section 5 are below the critical 2% threshold.

In the second example, the initial network design is an 8-branch parallel network with a microchannel volume fraction of 0.97%. The goal is minimizing the maximum temperature provided the microchannel volume fraction remains less than 0.125%. This constraint is initially violated, and as a result, we expect the optimizer to reduce the microchannel volume fraction in order to satisfy the constraint. To do so, the optimizer has three options: (i) reducing the number of branches; (ii) decreasing the diameter; and (iii) reducing the length of microchannels. Fig. 19(b and f) depict the

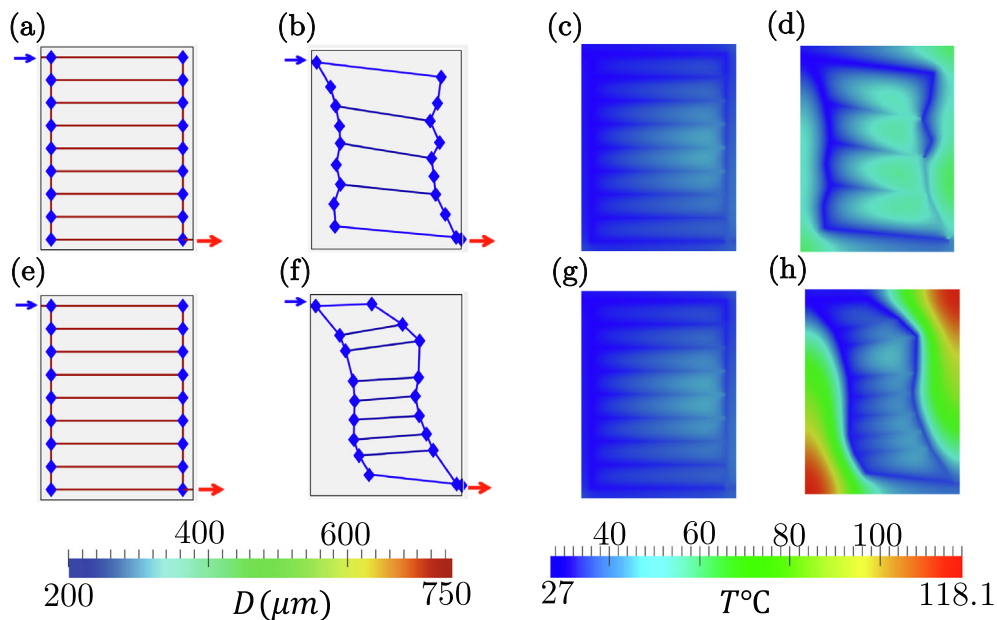


Fig. 19. HyTopS optimization: (a) initial, and (b) optimal designs and their respective temperature distributions (c, d). Shape optimization: (e) initial and (f) optimal designs and their respective temperature distributions (g, h). Note: the optimization problem is subjected to an initially violated constraint on the microchannel volume fraction ($V_{void} \leq 0.125\%$).

optimum design of the HyTopS optimization scheme and shape optimization method, respectively.

In the HyTopS approach, the optimizer decides to remove some of the microchannels as well as decrease existing microchannel diameters while keeping them long enough to reduce the maximum panel temperature to 62.4 °C as shown in Fig. 20. However, in the shape optimization method, the optimizer can only change the lengths and diameters of the microchannels. Consequently, it ends with a design exhibiting much lower performance in terms of maximum temperature (118.1 °C), as depicted in Fig. 20. In fact, the maximum panel temperature actually increases during the shape optimization process, which is not surprising since the volume fraction constraint is initially violated. To satisfy the purposely imposed strict constraints, the optimizer needed to decrease the number of branches, diameters, and lengths of the microchannels, which is not possible in the shape optimization approach.

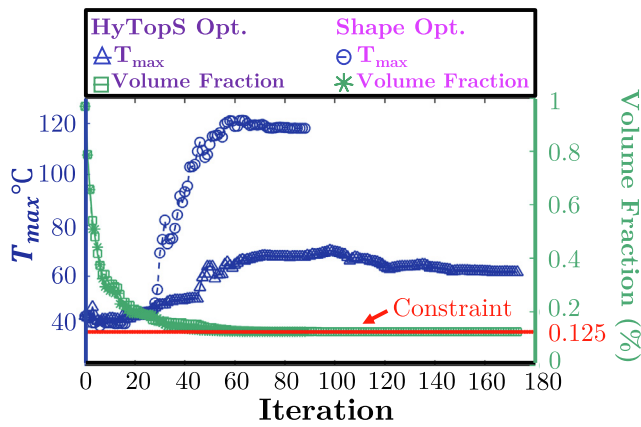


Fig. 20. Comparison between the maximum temperature history plots for the HyTopS and shape optimization methods. Both reference designs are 8-branch parallel networks that initially violate the imposed constraint on microchannel volume fraction ($V_{void} \leq 0.125\%$).

In the third and final example, the imposed constraint pertains to pressure drop, which is a critical consideration for practical microvascular fluid delivery since the required pressure for a given flow rate rapidly increases as the microchannel diameter decreases. Both the HyTopS and shape optimization methods are performed on an initial 2-branch parallel network as shown in Fig. 21(a and e), where the initial pressure drop is 18.9 KPa and the imposed constraint requires a pressure drop less than 16 KPa. As shown in Fig. 22, the obtained maximum panel temperature in the shape optimization scheme is 80.2 °C, only 0.7 °C lower than the initial design. However, the HyTopS optimization scheme created new microchannels in order to satisfy the pressure drop constraint while lowering the maximum panel temperature from 80.9 to 40 °C.

It is worth noting that in this example and throughout the paper, the optimization objective is related to thermal efficiency as opposed to flow efficiency. Thus the optimized vascular networks do not necessarily obey Murray's Law which states

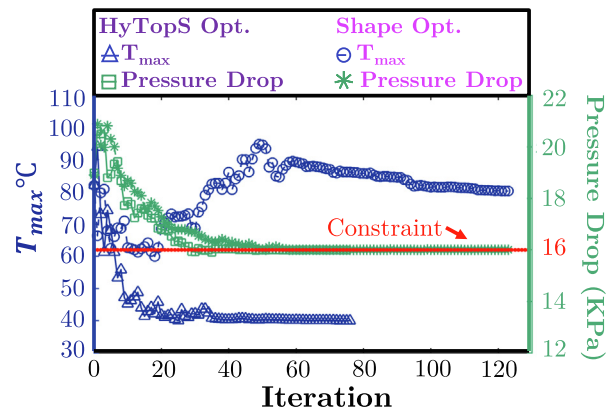


Fig. 22. Comparison between the maximum temperature history plots for the HyTopS and shape optimization methods. Both reference designs are 2-branch parallel networks that initially violate the imposed constraint on pressure drop ($\Delta P \leq 16$ KPa).

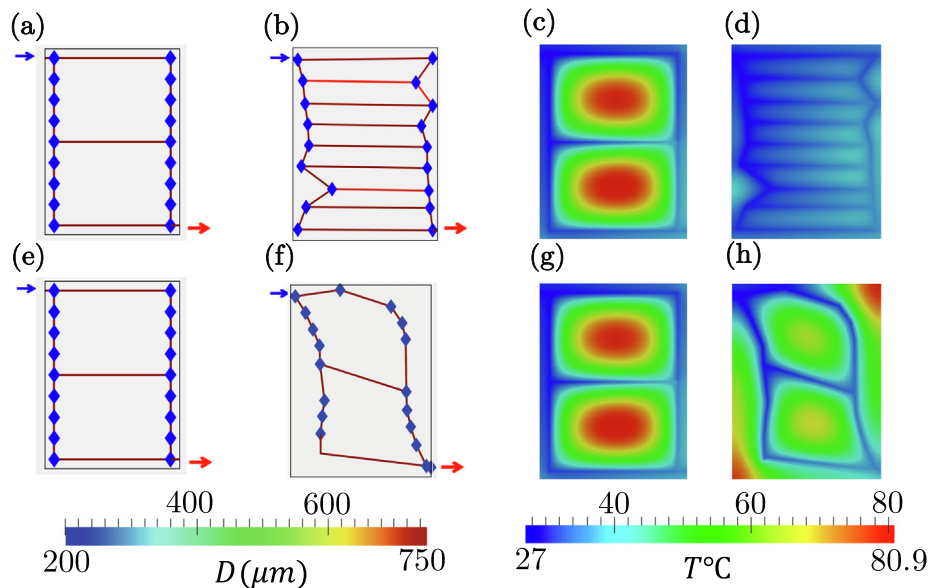


Fig. 21. HyTopS optimization: (a) initial, and (b) optimal designs and their respective temperature distributions (c, d). Shape optimization: (e) initial and (f) optimal designs and their respective temperature distributions (g, h). Note: the optimization problem is subjected to a constraint on the pressure drop ($\Delta P \leq 16$ KPa). In the HyTopS optimization scheme, the optimizer creates six new microchannels and satisfies the pressure drop constraint while significantly reducing the maximum panel temperature.

that maximum flow efficiency occurs when the sum of the radii cubed for parent and bifurcated children microchannels are equal [64]. In the future, we aim to optimize both thermal and flow efficiency.

6. Conclusion

In this study, we have presented a new gradient-based, hybrid topology/shape (HyTopS) optimization scheme for the design of readily manufacturable microvascular materials. By projecting the domain over a fixed mesh in the IGEM framework, our Eulerian approach eliminates mesh distortion issues commonly encountered in Lagrangian based methods and precisely captures the geometry of interest.

We have introduced a new set of design parameters that act analogous to the penalization factor defined in the SIMP method to create/remove microchannels and change the topology of the network during the optimization process. Furthermore, we have developed the analytical sensitivity of these design parameters and its accuracy is verified against finite difference method.

The computational cost is significantly reduced by utilizing IGEM and also using the simplified thermal and hydraulic models. In addition, taking advantage of the accurate representation of the microchannel boundaries and imposing a set of geometrical constraints, the resulting vascular network configurations are appropriate for large-scale manufacturing without performing any post-processing.

The method has been experimentally validated along with four metrics to quantify both steady-state and transient cooling performance. Two sets of application problems have been solved to demonstrate the advantages of using the proposed HyTopS approach for designing microvascular materials over shape optimization methods. We have shown that in contrast to a solely shape optimization approach, the design space in HyTopS is not limited to the topology of the initial configuration. Several examples have been solved to demonstrate the versatility of the HyTopS optimization method to handle strict manufacturing and fluid delivery constraints related to microvascular volume fraction and pressure drop.

While this study focused on active-cooling via heat-transport and fluid mechanics, we expect the numerical method and vascular fabrication approach will be applicable to a variety of physical phenomenon including structural and electromagnetic.

Declaration of Competing Interest

The authors declare no conflicts of interest.

Acknowledgements

The computational portion of this work has been financially supported by ‘start-up funds’ from Drexel University and the experimental portion by the Air Force Office of Scientific Research (grant # FA9550-18-1-0048). The authors acknowledge the high-performance computing resources (PROTEUS: the Drexel Cluster) and support at the Drexel University. The authors also extend their gratitude to the following: Dr. Ole Sigmund at the Technical University of Denmark for insightful research discussions; CU Aerospace LLC for providing VascTech printer filament; Sarah Mann for assistance with 3D printing and Zachary Phillips for assistance with the experimental setup. A.R.N. conceived the optimization approach while R.P. implemented the method computationally building upon a prior code developed by A.R.N. and M.H. Y.T. The experiments were conducted by S.H.A. and U.D. while W.H.M. helped construct the cooling setup and fabricate test samples, all under the direction of J.F.P. All authors participated in discussions of the research and wrote the manuscript.

Appendix A

A primary assumption behind the dimensionally reduced thermal model is that the mixed-mean fluid temperature T_m is approximately equal to the microchannel wall temperature T_w . To justify this assumption, we use the following equation, which is proposed in [4,52], to compute the difference between the mixed-mean fluid temperature and the wall temperature for fully developed, steady-state laminar flow,

$$\Delta T_{wm} \approx \frac{D_h^2 Q}{4A\kappa_c Nu L_{ch}}, \quad (A.1)$$

where D_h , Q , A , κ_c , Nu , and L_{ch} denote the hydraulic diameter of the microchannel, heat absorbed by the domain, the cross-sectional area of the microchannel, the thermal conductivity of the fluid, the Nusselt number, and the length of the microchannel, respectively.

We consider the optimum design presented in Section 4 for experimental validation. In that example, $Q = 15$ W, $L_{ch} = 1.27$ m, $D_h = 0.0005$ m, $\kappa_c = 0.419$ Wm⁻¹ K⁻¹, $A = 1.9635$ (10⁻⁷) m², and for fully developed fluid flow through a circular cross-section subjected to a constant heat flux, $Nu = 4.36$ [65]. Using these values, $\Delta T_{wm} \approx 2$ °C. Since in this analysis we assume that the total heat absorbed in the domain is removed by the microchannels, the actual difference would be less.

The second underlying assumption in this model is that the axial conduction of the coolant is negligible in comparison to the axial advection. To justify this assumption, we compute the Péclet number (Pe) which is equal to the ratio of advective to conductive heat transfer; the Péclet number is the product of the Reynolds number (Re) and the Prandtl number (Pr). Based on the values in the example of Section 4, $Re \approx 787$ and $Pr = 26.7$, and therefore $Pe \approx 21013 \gg 1$. Thus the advective term dominates and our assumption for neglecting axial conduction of the coolant is valid.

The third assumption pertains to the temperature-dependent dynamic viscosity (μ) of the coolant [21] and given by $\mu(T) = 0.0069(\frac{T}{273.15})^{-8.3}$ where the temperature T is expressed in Kelvin. To simplify the analysis, it is assumed that dynamic viscosity is uniform throughout the network and can be obtained from the average temperature of the microchannels, $\langle T \rangle = \frac{1}{|\Omega_f|} \int_{\Omega_f} T d\Omega_f$, where $|\Omega_f|$ is the total volume of the microchannels. We also assume that all of the other coolant and composite panel properties, i.e. specific heat capacity and thermal conductivity, are temperature independent.

Lastly, in the dimensionally reduced hydraulic model, the effect of microchannel corners on the pressure drop is ignored. As mentioned in [4], using this assumption may lead to almost 20% underestimation of the pressure drop within the microvascular network.

Appendix B

The Streamline Upwind Petrov–Galerkin (SUPG) method augments the weighting function in (1) to prevent solution instability due to the presence of the convective term, while the original weak form remains unchanged. Based on the SUPG method, weighting functions v in (1) will be replaced by weighting functions w as²:

$$w = v + \sum_{j=1}^{n_{ch}} \tau_e^{(j)} \mathbf{u}_{ave}^{(j)} \mathbf{t}^{(j)} \cdot \nabla v, \quad (B.1)$$

where

² In contrast to Bubnov-Galerkin based FEM, for the Petrov–Galerkin method the weighting functions are not identical to the shape functions.

$$\tau_e^{(j)} = \frac{h_e^{(j)}}{2u_{ave}^{(j)}} \left[\coth\left(\frac{u_{ave}^{(j)}h_e^{(j)}\rho_f c_f}{2\kappa}\right) - \frac{2\kappa}{u_{ave}^{(j)}h_e^{(j)}\rho_f c_f} \right], \quad (\text{B.2})$$

and

$$\frac{2}{h_e^{(j)}} = \sum_{k=1}^{n_{ch}} |\mathbf{t}^{(j)} \cdot \nabla N_k|, \quad (\text{B.3})$$

where ρ_f , u_{ave} , and N_k are the density of the fluid, the average velocity of the fluid, and the shape function associated with node k , respectively.

Eq. (B.1) can further be simplified due to the underlying physics of the problem. Based on the simulation parameters described in Section 4.1, $u_{ave}^{(j)}h_e^{(j)}\rho_f c_f/\kappa_f \approx 7000$. Thus, it can be assumed that $\text{Coth}\left(u_{ave}^{(j)}h_e^{(j)}\rho_f c_f/2\kappa_f\right) - \left(2\kappa_f/u_{ave}^{(j)}h_e^{(j)}\rho_f c_f\right) \approx 1$. Therefore:

$$\tau_e^{(j)} \approx \frac{h_e^{(j)}}{2u_{ave}^{(j)}}. \quad (\text{B.4})$$

Furthermore, linear triangular elements are employed in this study and as a result, $\nabla_{xx}v = 0$, and also, $\nabla_x w = \nabla_x v$. Note that the second term in (B.1), which is the streamline upwind contribution vanishes at the boundaries. Thus, after applying all these simplifications, (B.1) can be written as the following:

$$w = v + \sum_{j=1}^{n_{ch}} \frac{h_e^{(j)}}{2} \mathbf{t}^{(j)} \cdot \nabla v. \quad (\text{B.5})$$

Using (B.5), the SUPG weighting function can be discretized analogous to (2) as:

$$W^h(\mathbf{X}) = \mathbb{W}^e(\mathbf{X})V^e, \quad (\text{B.6})$$

where

$$\mathbb{W}^e = \mathbb{N}^e + \sum_{j=1}^{n_{ch}} \frac{h_e^{(j)}}{2} \mathbf{t}^{(j)} \mathbb{B}^e. \quad (\text{B.7})$$

Appendix C

As mentioned in Section 3, we define a threshold mass flow rate for which the optimizer will remove microchannels with flow rates below the threshold. This removal must have a negligible effect on the value of the objective function. To demonstrate the procedure for finding a mass flow rate threshold, we solve an illustrative example. An 8-branch parallel network with the same simulation parameters, material properties, and boundary conditions of the example in Section 5 is considered. The mass flow rate of the middle microchannel in Fig. C23(a) is augmented to investigate its

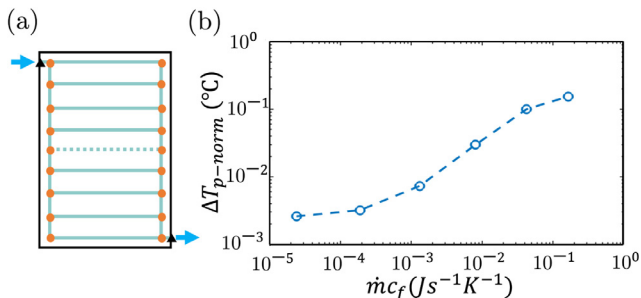


Fig. C23. (a) 8-branch parallel network. The dashed line indicates a microchannel whose mass flow rate is changed to illustrate its effect on the objective value, (b) Plot showing the difference in the temperature p -norm of the domain versus m_c_f by retaining or removing the selected microchannel.

effect on the objective value (temperature p -norm). For this problem, when m_c_f is less than 10^{-3} , the difference between the temperature p -norm of the network with and without the respective microchannel is practically negligible ($<0.02\%$), as shown in Fig. C23(b). Note that the effect of this microchannel removal on the pressure drop of the network, mass flow rates of the other microchannels, and on the nodal pressures is also negligible.

Appendix D

The partial derivative of (B.7) with respect to α_i is as follows:

$$\frac{\partial \mathbb{W}^e}{\partial \alpha_i} = \frac{\partial \mathbb{N}^e}{\partial \alpha_i} + \frac{1}{2} \sum_{j=1}^{n_{ch}} \left(\frac{\partial h_e^{(j)}}{\partial \alpha_i} \mathbf{t}^{(j)} \mathbb{B}^e + h_e^{(j)} \mathbf{t}^{(j)} \frac{\partial \mathbb{B}^e}{\partial \alpha_i} + h_e^{(j)} \frac{\partial \mathbf{t}^{(j)}}{\partial \alpha_i} \mathbb{B}^e \right), \quad (\text{D.1})$$

where

$$\frac{\partial h_e^{(j)}}{\partial \alpha_i} = -\frac{h_e^{(j)2}}{2} \sum_{k=1}^{n_{ch}} \text{sign}(\mathbb{B}_k^e \mathbf{t}^{(j)}) \left(\mathbf{t}^{(j)} \left(\frac{\partial \mathbb{B}_k^e}{\partial \alpha_i} \right)' + \frac{\partial \mathbf{t}^{(j)}}{\partial \alpha_i} \mathbb{B}_k^e \right), \quad (\text{D.2})$$

and

$$\mathbb{B}_k^e = \left[\frac{\partial \mathbb{N}_k^e}{\partial x} \quad \frac{\partial \mathbb{N}_k^e}{\partial y} \right]. \quad (\text{D.3})$$

As mentioned earlier in Section 3.1, $\partial \mathbb{N}^e / \partial \alpha_i$, $\partial \mathbf{t}^{(j)} / \partial \alpha_i$ and $\partial \mathbb{B}^e / \partial \alpha_i$ are zero, therefore, $\partial h_e^{(j)} / \partial \alpha_i$ becomes zero. As a result, all of the terms on the right-hand side of (D.1) vanish, i.e., $\partial \mathbb{W}^e / \partial \alpha_i = 0$.

References

- [1] J.F. Patrick, M.J. Robb, N.R. Sottos, J.S. Moore, S.R. White, Polymers with autonomous life-cycle control, *Nature* 540 (2016) 363–370.
- [2] A.P. Esser-Kahn, P.R. Thakre, H. Dong, J.F. Patrick, V.K. Vlasko-Vlasov, N.R. Sottos, J.S. Moore, S.R. White, Three-dimensional microvascular fiber-reinforced composites, *Adv. Mater.* 23 (32) (2011) 3654–3658.
- [3] S.J. Pety, M.H.Y. Tan, A.R. Najafi, P.R. Barnett, P.H. Geubelle, S.R. White, Carbon fiber composites with 2D microvascular networks for battery cooling, *Int. J. Heat Mass Transf.* 115 (2017) 513–522.
- [4] M.H.Y. Tan, A.R. Najafi, S.J. Pety, S.R. White, P.H. Geubelle, Gradient-based design of actively-cooled microvascular composite panels, *Int. J. Heat Mass Transf.* 103 (2016) 594–606.
- [5] A.M. Coppola, A.S. Griffin, N.R. Sottos, S.R. White, Retention of mechanical performance of polymer matrix composites above the glass transition temperature by vascular cooling, *Compos. Part A: Appl. Sci. Manuf.* 78 (2015) 412–423.
- [6] B.D. Kozola, L.A. Shipton, V.K. Natrajan, K.T. Christensen, S.R. White, Characterization of active cooling and flow distribution in microvascular polymers, *J. Intell. Mater. Syst. Struct.* 21 (12) (2010) 1147–1156.
- [7] D.M. Phillips, R.M. Pierce, J. Baur, Mechanical and thermal analysis of microvascular networks in structural composite panels, *Compos. Part A: Appl. Sci. Manuf.* 42 (11) (2011) 1609–1619.
- [8] D.M. Phillips, J.W. Baur, A microvascular method for thermal activation and deactivation of shape memory polymers, *J. Intell. Mater. Syst. Struct.* 24 (10) (2013) 1233–1244.
- [9] A. Bejan, Constructal-theory network of conducting paths for cooling a heat generating volume, *Int. J. Heat Mass Transf.* 40 (4) (1997) 799–816.
- [10] Y. Hadad, B. Ramakrishnan, R. Pejman, S. Rangarajan, P.R. Chiarot, A. Pattamatta, B. Sammakia, Three-objective shape optimization and parametric study of a micro-channel heat sink with discrete non-uniform heat flux boundary conditions, *Appl. Therm. Eng.* 150 (2019) 720–737.
- [11] L. Chai, G.D. Xia, H.S. Wang, Parametric study on thermal and hydraulic characteristics of laminar flow in microchannel heat sink with fan-shaped ribs on sidewalls—Part 3: Performance evaluation, *Int. J. Heat Mass Transf.* 97 (2016) 1091–1101.
- [12] J.H. Ryu, D.H. Choi, S.J. Kim, Three-dimensional numerical optimization of a manifold microchannel heat sink, *Int. J. Heat Mass Transfer* 46 (9) (2003) 1553–1562.
- [13] Y. Hadad, R. Pejman, B. Ramakrishnan, P.R. Chiarot, B.G. Sammakia, Geometric optimization of an impinging cold-plate with a trapezoidal groove used for warm water cooling, in: 2018 17th IEEE Intersociety Conference on Thermal and Thermomechanical Phenomena in Electronic Systems (ITherm), IEEE, 2018, pp. 673–682.
- [14] S. Soghrati, A.R. Najafi, J.H. Lin, K.M. Hughes, S.R. White, N.R. Sottos, P.H. Geubelle, Computational analysis of actively-cooled 3D woven microvascular

- composites using a stabilized interface-enriched generalized finite element method, *Int J Heat Mass Tran* 65 (2013) 153–164.
- [15] D.E. Goldberg, *Genetic Algorithms in Search, Optimization & Machine Learning*, 1988.
- [16] P. Li, Y. Liu, T. Zou, J. Huang, Optimal design of microvascular networks based on non-dominated sorting genetic algorithm II and fluid simulation, *Adv. Mech. Eng.* 9 (7) (2017), 1687814017708175.
- [17] S. Soghrati, A.M. Aragón, P.H. Geubelle, Design of actively-cooled microvascular materials: a genetic algorithm inspired network optimization, *Struct. Multidiscip. Optim.* 49 (4) (2014) 643–655.
- [18] A.M. Aragón, R. Saksena, B.D. Kozola, P.H. Geubelle, K.T. Christensen, S.R. White, Multi-physics optimization of three-dimensional microvascular polymeric components, *J. Comput. Phys.* 233 (2013) 132–147.
- [19] A.M. Aragón, K.J. Smith, P.H. Geubelle, S.R. White, Multi-physics design of microvascular materials for active cooling applications, *J. Comput. Phys.* 230 (13) (2011) 5178–5198.
- [20] A.M. Aragón, J.K. Wayer, P.H. Geubelle, D.E. Goldberg, S.R. White, Design of microvascular flow networks using multi-objective genetic algorithms, *Comput. Methods Appl. Mech. Eng.* 197 (49–50) (2008) 4399–4410.
- [21] A. Jarrett, I.Y. Kim, Design optimization of electric vehicle battery cooling plates for thermal performance, *J. Power Sources* 196 (23) (2011) 10359–10368.
- [22] M.H.Y. Tan, A.R. Najafi, S.J. Pety, S.R. White, P.H. Geubelle, Multi-objective design of microvascular panels for battery cooling applications, *Appl. Therm. Eng.* 135 (2018) 145–157.
- [23] M.H.Y. Tan, D. Bunce, A.R. Ghosh, P.H. Geubelle, Computational design of microvascular radiative cooling panels for nanosatellites, *J. Thermophys. Heat Transfer* 32 (3) (2018) 605–616.
- [24] S.J. Pety, M.H.Y. Tan, A.R. Najafi, A.C. Gendusa, P.R. Barnett, P.H. Geubelle, S.R. White, Design of redundant microvascular cooling networks for blockage tolerance, *Appl. Therm. Eng.* 131 (2018) 965–976.
- [25] A.R. Najafi, M. Safdari, D.A. Tortorelli, P.H. Geubelle, Shape optimization using a NURBS-based interface-enriched generalized FEM, *Int. J. Numer. Meth. Eng.* 111 (10) (2017) 927–954.
- [26] A.R. Najafi, M. Safdari, D.A. Tortorelli, P.H. Geubelle, A gradient-based shape optimization scheme using an interface-enriched generalized FEM, *Comput. Methods Appl. Mech. Eng.* 296 (2015) 1–17.
- [27] S. Soghrati, A.M. Aragón, C. Armando Duarte, P.H. Geubelle, An interface-enriched generalized FEM for problems with discontinuous gradient fields, *Int. J. Numer. Meth. Eng.* 89 (8) (2012) 991–1008.
- [28] M. Safdari, A.R. Najafi, N.R. Sottos, P.H. Geubelle, A NURBS-based interface-enriched generalized finite element method for problems with complex discontinuous gradient fields, *Int. J. Numer. Meth. Eng.* 101 (12) (2015) 950–964.
- [29] T. Borrvall, J. Petersson, Topology optimization of fluids in Stokes flow, *Int. J. Num. Methods Fluids* 41 (1) (2003) 77–107.
- [30] A. Gersborg-Hansen, M.P. Bendsoe, O. Sigmund, Topology optimization of heat conduction problems using the finite volume method, *Struct. Multidiscip. Optim.* 31 (4) (2006) 251–259.
- [31] T. Matsumori, T. Kondoh, A. Kawamoto, T. Nomura, Topology optimization for fluid–thermal interaction problems under constant input power, *Struct. Multidiscip. Optim.* 47 (4) (2013) 571–581.
- [32] X. Zhao, M. Zhou, O. Sigmund, C.S. Andreasen, A “poor man’s approach” to topology optimization of cooling channels based on a Darcy flow model, *Int. J. Heat Mass Transf.* 116 (2018) 1108–1123.
- [33] M. Zhou, B.S. Lazarov, F. Wang, O. Sigmund, Minimum length scale in topology optimization by geometric constraints, *Comput. Methods Appl. Mech. Eng.* 293 (2015) 266–282.
- [34] M.P. Bendsoe, O. Sigmund, Material interpolation schemes in topology optimization, *Archive Appl. Mech.* 69 (9–10) (1999) 635–654.
- [35] M.P. Bendsoe, N. Kikuchi, Generating optimal topologies in structural design using a homogenization method, *Comput. Methods Appl. Mech. Eng.* 71 (2) (1988) 197–224.
- [36] P. Duysinx, L. Van Mieghroet, T. Jacobs, C. Fleury, Generalized shape optimization using X-FEM and level set methods, in: *IUTAM Symposium on Topological Design Optimization of Structures, Machines and Materials*, Springer, 2006, pp. 23–32.
- [37] L. Van Mieghroet, N. Moës, C. Fleury, P. Duysinx, Generalized shape optimization based on the level set method, in: *Proceedings of the 6th World Congress of Structural and Multidisciplinary Optimization (WCSMO6)*, 2005.
- [38] S. Soghrati, P.H. Geubelle, A 3D interface-enriched generalized finite element method for weakly discontinuous problems with complex internal geometries, *Comput. Methods Appl. Mech. Eng.* 217–220 (2012) 46–57.
- [39] M. Safdari, A.R. Najafi, N.R. Sottos, P.H. Geubelle, A NURBS-based generalized finite element scheme for 3D simulation of heterogeneous materials, *J. Comput. Phys.* 318 (2016) 373–390.
- [40] I. Babuška, U. Banerjee, Stable generalized finite element method (SGFEM), *Comput. Methods Appl. Mech. Eng.* 201 (2012) 91–111.
- [41] T. Belytschko, R. Gracie, G. Ventura, A review of extended/generalized finite element methods for material modeling, *Model Simul. Mater. Sci. Eng.* 17 (4) (2009) 043001.
- [42] M.H.Y. Tan, M. Safdari, A.R. Najafi, P.H. Geubelle, A NURBS-based interface-enriched generalized finite element scheme for the thermal analysis and design of microvascular composites, *Comput. Methods Appl. Mech. Eng.* 283 (1) (2015) 1382–1400.
- [43] A.N. Brooks, T.J. Hughes, Streamline upwind/Petrov-Galerkin formulations for convection dominated flows with particular emphasis on the incompressible Navier–Stokes equations, *Comput. Methods Appl. Mech. Eng.* 32 (1–3) (1982) 199–259.
- [44] M. Bahrami, M.M. Yovanovich, J.R. Culham, Pressure drop of fully-developed, laminar flow in microchannels of arbitrary cross-section, in: *ASME 3rd International Conference on Microchannels and Minichannels*, American Society of Mechanical Engineers, 2008, pp. 269–280.
- [45] R.K. Shah, A.L. London, *Laminar flow forced convection in ducts (a sourcebook for compact heat transfer exchange analytical data)*, 1978.
- [46] J.A. Norato, B.K. Bell, D.A. Tortorelli, A geometry projection method for continuum-based topology optimization with discrete elements, *Comput. Methods Appl. Mech. Eng.* 293 (2015) 306–327.
- [47] C. Le, J. Norato, T. Bruns, C. Ha, D. Tortorelli, Stress-based topology optimization for continua, *Struct. Multidiscip. Optim.* 41 (4) (2010) 605–620.
- [48] P. Duysinx, O. Sigmund, developments in handling stress constraints in optimal material distribution, in: *7th AIAA/USAF/NASA/ISSMO Symposium on Multidisciplinary Analysis and Optimization*, 1998, p. 4906.
- [49] R.J. Yang, C.J. Chen, Stress-based topology optimization, *Struct. Optim.* 12 (2–3) (1996) 98–105.
- [50] D.A. Dunavnt, High degree efficient symmetrical Gaussian quadrature rules for the triangle, *Int. J. Num. Methods Eng.* 21 (6) (1985) 1129–1148.
- [51] S. Soghrati, P.R. Thakre, S.R. White, N.R. Sottos, P.H. Geubelle, Computational modeling and design of actively-cooled microvascular materials, *Int. J. Heat Mass Transf.* 55 (19–20) (2012) 5309–5321.
- [52] M.H.Y. Tan, P.H. Geubelle, 3D dimensionally reduced modeling and gradient-based optimization of microchannel cooling networks, *Comput. Methods Appl. Mech. Eng.* 323 (2017) 230–249.
- [53] J.F. Patrick, B.P. Krull, M. Garg, C.L. Mangun, J.S. Moore, N.R. Sottos, S.R. White, Robust sacrificial polymer templates for 3D interconnected microvasculature in fiber-reinforced composites, *Compos. Part A: Appl. Sci. Manuf.* 100 (2017) 361–370.
- [54] G. Zhang, S.G. Kandlikar, A critical review of cooling techniques in proton exchange membrane fuel cell stacks, *Int. J. Hydrogen Energy* 37 (3) (2012) 2412–2429.
- [55] ASTM International, *ASTM E1356: Standard Test Method for Assignment of the Glass Transition Temperatures by Differential Scanning Calorimetry*, 2014.
- [56] ASTM International, *ASTM D3171: Standard Test Methods for Constituent Content of Composite Materials*, 2015.
- [57] D.J. Hartl, G.J. Frank, J.W. Baur, Effects of microchannels on the mechanical performance of multifunctional composite laminates with unidirectional laminae, *Compos. Struct.* 143 (2016) 242–254.
- [58] A.M. Coppola, P.R. Thakre, N.R. Sottos, S.R. White, Tensile properties and damage evolution in vascular 3D woven glass/epoxy composites, *Compos. Part A: Appl. Sci. Manuf.* 59 (2014) 9–17.
- [59] C.-Y. Huang, R. Trask, I. Bond, Characterization and analysis of carbon fibre-reinforced polymer composite laminates with embedded circular vasculature, *J. Roy. Soc. Interface* 7 (49) (2010) 1229–1241.
- [60] A. Kousourakis, M.K. Bannister, A.P. Mouritz, Tensile and compressive properties of polymer laminates containing internal sensor cavities, *Compos. Part A: Appl. Sci. Manuf.* 39 (9) (2008) 1394–1403.
- [61] C.J. Norris, I.P. Bond, R.S. Trask, Interactions between propagating cracks and bioinspired self-healing vasculature embedded in glass fibre reinforced composites, *Compos. Sci. Technol.* 71 (6) (2011) 847–853.
- [62] C.J. Norris, I.P. Bond, R.S. Trask, The role of embedded bioinspired vasculature on damage formation in self-healing carbon fibre reinforced composites, *Compos. Part A: Appl. Sci. Manuf.* 42 (6) (2011) 639–648.
- [63] A. Kousourakis, A.P. Mouritz, M.K. Bannister, Interlaminar properties of polymer laminates containing internal sensor cavities, *Compos. Struct.* 75 (1–4) (2006) 610–618.
- [64] C.D. Murray, The physiological principle of minimum work: I. The vascular system and the cost of blood volume, *Proc. Nat. Acad. Sci. USA* 12 (3) (1926) 207–214.
- [65] W.M. Kays, M.E. Crawford, B. Weigand, *Convective Heat and Mass Transfer*, McGraw-Hill, 2005.